



DEPAUL UNIVERSITY

STATIC FOURIER TRANSFORM SPECTROSCOPY  
AND  
DATA MINING TIME-RESOLVED SMALL PATH-DIFFERENCE  
INTERFEROGRAMS

A THESIS SUBMITTED TO  
THE FACULTY OF THE COLLEGE OF SCIENCE AND HEALTH  
IN CANDIDACY FOR THE DEGREE OF  
MASTER OF SCIENCE

THE DEPARTMENT OF PHYSICS

BY

MATT RAYMOND

CHICAGO, ILLINOIS

SEPTEMBER 2015

*Thank you, for lots of things*

Dr. Stefan Catoi

Dr. Chris Goedde

Dr. Eric Landahl

Dr. Richard Niedziela

Dr. Rubin Parra

Dr. Catherine Southern

# Contents

<b>1. Introduction</b>	<b>1</b>
<b>2. Constructing the Interferometer</b>	<b>7</b>
2.1 Stage 1: Coarse Positioning and Alignment with HeNe Lasers . . . . .	7
2.2 Stage 2: Vibrations, Collimation, and Progressively Finer Alignments . . . . .	10
2.2.1 Vibrations . . . . .	10
2.2.2 Collimation . . . . .	11
2.2.3 Progressively Finer Alignments and Summary . . . . .	13
2.3 Construction: Step-by-Step Using Breadboards . . . . .	13
2.4 Construction: Step-by-Step Using Magnetic Bases . . . . .	17
2.5 Parts Used in Constructing the Interferometer . . . . .	20
2.6 Measurements: The Instrument, Settings, and Labeling Samples . . . . .	23
<b>3. Fourier Transform Mathematics</b>	<b>25</b>
3.1 The Physical Interpretation . . . . .	26
3.2 Background and Definitions: Topologies and Measure Spaces . . . . .	28
3.3 Background and Definitions: Lebesgue Integration and $L^p$ Spaces . . . . .	30
3.4 Background and Definitions: Lebesgue Measure . . . . .	33
3.5 Results: from Measure Theory . . . . .	34
3.5.1 Fourier Transforms in $L^1$ . . . . .	35
3.5.2 Fourier Transforms in $L^2$ : The Plancherel Transformation . . . . .	35
3.5.3 Fourier Series . . . . .	36
3.6 Results: from Functional Analysis . . . . .	38
3.6.1 Fourier Transforms of Rapidly Decreasing Functions . . . . .	39
3.6.2 Fourier Transforms of Distributions . . . . .	41
3.7 Using Distributions: Efficient Fourier Transform Calculations . . . . .	42
3.8 Using Distributions: Estimating the Resolution of the Spectrometer . . . . .	43
<b>4. From Signal to Spectra</b>	<b>45</b>
4.1 Locating An Interferogram's Axis of Symmetry . . . . .	47

4.2	Apodization . . . . .	52
4.3	Implementing The Discrete Fourier Transform . . . . .	53
4.4	Interpolation . . . . .	55
4.5	Spectra and Units . . . . .	60
<b>5.</b>	<b>Results and Discussion: Measured Spectra</b>	<b>63</b>
5.1	Calibrations with HeNe and Na Spectra . . . . .	64
5.2	Comparisons with Known Spectra . . . . .	67
<b>6.</b>	<b>Results and Discussion: Data Mining</b>	<b>69</b>
6.1	Qualitative Trends . . . . .	69
6.2	Probabilistic Modeling and Statistical Significance . . . . .	77
6.3	Quantitative Results . . . . .	78
<b>7.</b>	<b>Conclusions</b>	<b>85</b>

## List of Figures

1.0.1	Standard Fourier Transform Spectrometer Ray Diagram . . . . .	1
1.0.2	Static Fourier Transform Spectrometer Ray Diagram . . . . .	1
1.0.3	A Histogram of Hg Interferogram Measurements Over Time . . . . .	4
2.1.1	HeNe Diffraction and Interference Produced in the Lab . . . . .	8
2.1.2	HeNe Interference in Orienting Optics . . . . .	8
2.1.3	An Adjustable HeNe Laser Fastened to a Mirror Mount . . . . .	9
2.1.4	The Distance Replicator and the Predator-Style System of HeNe Lasers . . . . .	9
2.2.1	The Collimator . . . . .	11
2.2.2	Aligning the Collimator . . . . .	12
2.3.1	Breadboard Construction 1: Fastening Holds and HeNe Alignment . . . . .	14
2.3.2	Breadboard Construction 2: The Mirror on the Precision Stage . . . . .	15
2.3.3	Breadboard Construction 3: The Beamsplitter, Compensator, and Coarse Stage . . .	15
2.3.4	Breadboard Construction 4: Final Alignments . . . . .	16
2.4.1	Magnetic Base Construction 1: The First Holds and HeNe Alignment . . . . .	17
2.4.2	Magnetic Base Construction 2: Replicating Distances with the PS System . . . . .	18
2.4.3	Magnetic Base Construction 3: Making a Right-Angle With the Distance Replicator	18
2.4.4	Magnetic Base Construction 4: A HeNe Trace of the Second Interferometer Arm . . .	19
2.4.5	Magnetic Base Construction 5: The Precision Stage . . . . .	19
2.4.6	Magnetic Base Construction 6: The Completed Interferometer . . . . .	20
2.5.1	Manufacturer’s Specifications on the Mirrors and Beam Splitter . . . . .	21
2.5.2	The Beamsplitter’s Ray Diagram: Reflected and Transmitted Paths . . . . .	21
2.5.3	The Beamsplitter and Compensator Used in the Experiment . . . . .	22
2.6.1	The Detector: The Thorlabs LC100 Linear CCD Array . . . . .	23
2.6.2	Interference Produced with Na and Hg Discharge Tubes and White Light . . . . .	24
4.0.1	Signal Processing Flow Chart: Complete From Signal To Spectra . . . . .	45
4.0.2	Signal Processing Flow Chart: The First Steps and Their Effects . . . . .	46
4.1.1	Estimated Interferogram Axes of Symmetry: Examples 1 . . . . .	47
4.1.2	Interferogram Axes of Symmetry: The Process of Estimating . . . . .	48

4.1.3	Estimated Interferogram Axes of Symmetry: Examples 2 . . . . .	51
4.1.4	Signal Processing Flow Chart: Measurement to Symmetry Estimates . . . . .	52
4.2.1	Signal Processing Flow Chart: Measurement to Apodization . . . . .	52
4.2.2	The Effects of Apodization . . . . .	53
4.3.1	Signal Processing Flow Chart: Measurement to the DFT . . . . .	54
4.4.1	Signal Processing Flow Chart: Measurement to Interpolation . . . . .	56
4.4.3	Interpolation: Zero Filling Exemplified with a HeNe Interferogram . . . . .	58
4.4.4	Interpolation: Mirror Imaging Exemplified with a HeNe Interferogram . . . . .	60
4.5.1	Signal Processing Flow Chart: Complete From Signal To Spectra . . . . .	61
5.1.1	A Measured HeNe Interferogram and its Spectra by FT . . . . .	65
5.2.1	Comparing the Spectra from Measured Interferograms to Known Values . . . . .	67
5.2.2	The lightbulb's Spectra by FT . . . . .	68
6.1.1	Data Mining: Processing of the Spatial Domain Histograms . . . . .	70
6.1.2	Spatial Domain Histograms: Examples . . . . .	71
6.1.3	Spatial Domain Histograms: A Close Up on the Lightbulb . . . . .	72
6.1.4	Data Mining: Processing of the Time Domain Histograms . . . . .	72
6.1.5	Time Domain Histograms: Examples . . . . .	73
6.1.6	Spatial Averaged Intensities: Examples 1 . . . . .	74
6.1.7	Spatial Averaged Intensities: Examples 2 . . . . .	75
6.1.8	Plots of Complex Fourier Transformed Coefficients: Examples . . . . .	76
6.2.1	A Probabilistic Model for Identifying Samples . . . . .	77
6.3.1	Data Mining: Quantifying Time Variations in Intensity Measurements . . . . .	79
6.3.4	Data Mining: Quantifying Time Discontinuities in Measured Intensities . . . . .	81
6.3.7	Data Mining: Quantifying Band Gaps in Intensity Measurements . . . . .	83

## List of Tables

5.2.3	Quantitatively Comparing Measured and Known Spectra . . . . .	68
6.3.2	Time Variations in Intensity Measurements: Descriptive Statistics by Sample Type .	79
6.3.3	Estimating Sample Type by Time Variations in Intensity Measurements . . . . .	80
6.3.5	Time Discontinuities in Intensity Measurements: Descriptive Statistics by Sample Type	81
6.3.6	Estimating Sample Type by Time Discontinuities in Intensity Measurements . . . . .	82
6.3.8	Band Gaps in Intensity Measurements: Descriptive Statistics by Sample Type . . . .	84
6.3.9	Estimating Sample Type by Band Gaps in Intensity Readings . . . . .	84

# Abbreviations

DFT                    *Discrete Fourier transform*

DR                    *The distance replicator*

EM                    *Electromagnetic*

FA                    *The fixed-height aperture*

FT                    *Fourier transform*

H                    *Hydrogen*

HeNe                    *Helium-neon Laser*

Hg                    *Mercury*

IR                    *Infrared*

LB                    *Lightbulb*

Na                    *Sodium*

PS System                    *The predator-style system*

UV-Vis                    *Ultra-violet and visible*



# Mathematical Symbols

$\hat{f}$	<i>The Fourier transform of <math>f</math></i>
$\in$	<i>In</i>
$\forall$	<i>For all</i>
$\implies$	<i>Implies</i>
<i>iff</i>	<i>If and only if</i>
$\mathbf{N}, \mathbf{N}^+$	<i>The integers, the positive integers</i>
$\mathbf{R}$	<i>The real numbers</i>
$\mathbf{C}$	<i>The complex numbers</i>
$1_A$	<i>The indicator function on the set <math>A</math></i>
$A^c$	<i>The compliment of the set <math>A</math></i>
$\mu$	<i>An arbitrary measure</i>
$m$	<i>The Lebesgue measure (or one proportional to it)</i>
$\mathcal{F}$	<i>A sigma algebra</i>

# 1 Introduction

---

The capability of making time-resolved measurements of interferograms has recently become possible with the advent of high-precision CCD arrays. A natural step is then to replace the standard single detector and linear actuator system used in Fourier transform (FT) spectroscopy

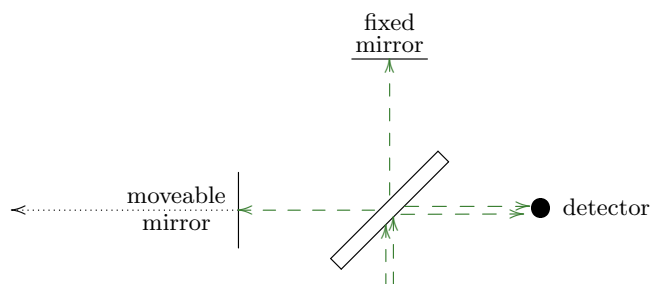


Fig. 1.0.1: In a standard FT spectrometer, a single detector measures the intensity produced by a Michelson interferometer as a moveable mirror steps laterally to alter the path difference.

with a linear CCD array and a little bit of mirror tilt.

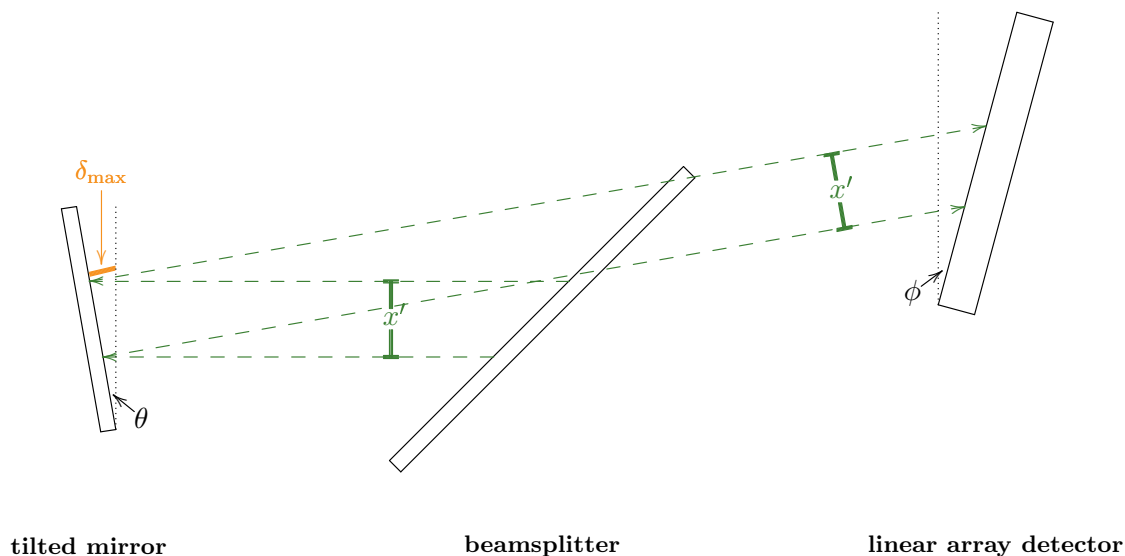


Fig. 1.0.2: In a static FT spectrometer a path difference is created by tilting one of the interferometer mirrors (angles are exaggerated). The linear array detector then makes simultaneous measurements of the entire interferogram: in our case every 5 *ms*. The symbol  $\delta_{\max}$  is used to indicate the maximum path difference introduced by the tilted mirror.

This particular static design has been studied by Aryamana-Mugisha and Williams and Shardt et al. for applications in the UV-Vis and IR, respectively, however there are many variations on the theme [1, 2]. By far the most common is to substitute the beamsplitter with Wollaston prisms, where the birefringence has the added effect of introducing a varying path difference along the width of the beam, and to make measurements using a 2D array detector (used by Shardt et al. as well) [3, 4, 5, 6, 2]. Boer et al. have also incorporated a set of planar liquid crystal polarizers to alter the birefringent behavior of the prisms [3]. Alternatively Lacan et al. kept the beamsplitter but instead incorporated a stepped mirror, to circumvent the asymmetry at recombination that's been exaggerated in the figure above, and a 2D detector [7]. A more drastic variation is found with Zhan where the Michelson interferometer was replaced by a Sagnac with spherical reflectors [8].

The main engineering benefits of the static design come from avoiding costs, alignments, real-time maintenance, and the measurement times associated with high-precision linear actuators. Similarly there is an innate stability in having no moving parts: Lacan et al. placed these on micro satellites to study CO<sub>2</sub> concentrations, and Hegyi's study focused on applications for motion detection ranging from flow cytometers to fixed-wing aircraft to nanosatellites<sup>1</sup> [4, 7]. Compactness is also a theme, and a more extreme case is Patterson et al.'s which was built within a 40 mm cube (slightly larger than a golf-ball) [6].

As mentioned at the outset, there is also a benefit as the instrument is recording a new kind of data: time-resolved interferograms. To see how this plays out, let  $E_\lambda(x, t)$  be a theoretical one-dimensional EM wave of wavelength  $\lambda$ . After a path difference  $\delta$  is introduced, the beam recombines with itself producing

$$E_{\lambda, \delta}(x, t) = E_\lambda(x, t) + E_\lambda(x + \delta, t)$$

As the path difference is varied, the optics are then performing a periodic mapping  $(E_\lambda, \delta) \rightarrow E_{\lambda, \delta}$  that has wavelength  $\lambda$  with respect to  $\delta$ .

---

<sup>1</sup>Nanosatellites are defined as weighing 1 – 10 kg.

In the standard case involving a linear actuator, the moving mirror is briefly held fixed and the average intensity of the recombined beam  $\bar{I}_\lambda(\delta)$  is measured. The mirror then moves to introduce a new path difference, the process is repeated, and all together the measurement process can be represented as the composition  $(E_\lambda, \delta) \rightarrow E_{\lambda, \delta} \rightarrow \bar{I}_\lambda$  which also has wavelength  $\lambda$ . This average intensity  $\bar{I}_\lambda$  of the recombined beam is constant over short distances and can be measured with a detector. Thus the instrument transfers the burden of creating something small enough to measure within the wavelength of our initial EM wave  $E_\lambda$  to the precise motion of a mirror controlling  $\delta$ . In the more general case our initial EM wave would be some sum  $E = \sum E_\lambda$ 's and for non-coherent sources we can approximate the resulting average intensity as  $\bar{I} = \sum \bar{I}_\lambda$ . Fourier transformation of this  $\bar{I}$  then attempts to determine the initial composition.

The set of measurements just described something like  $\{\bar{I}(\delta): 0 \leq \delta \leq \delta_{\max}\}$ . However in the static case this whole set of measurements is collected simultaneously, and this is done repeatedly over time. Therefore the static set of measurements has an extra dimension to it  $\{\bar{I}(\delta, t): 0 \leq \delta \leq \delta_{\max}, 0 \leq t \leq t_{\max}\}$ . We can easily average these over time<sup>1</sup> and get the standard measurements that we can FT, but this is throwing out information (particularly with our detector outputting the entire interferogram every 5 *ms*). This is illustrated in the figure below.

---

<sup>1</sup>The individual measurements  $\bar{I}(\delta, t)$  are still time averaged as the detector doesn't behave instantaneously so we're keeping the bar in the notation.

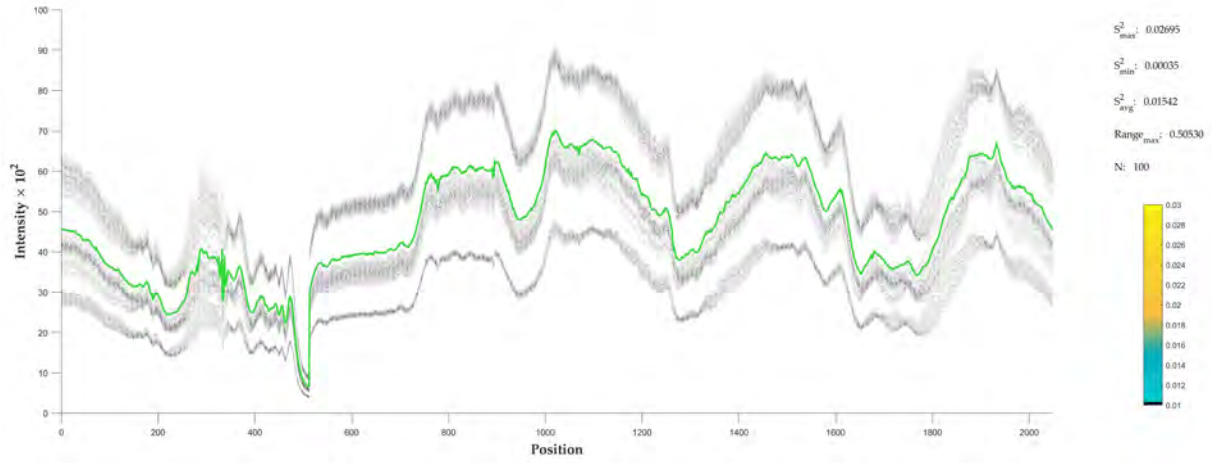


Fig. 1.0.3: A histogram of readings from an Hg arc lamp. The black dots comprise the static's measurements  $\bar{I}(\delta, t)$  while the time average of this set, the thin green line, is what's measured by a standard FT spectrometer. The apparent band gaps alone, which were largest with Hg, were found capable of distinguishing the sources used here with 95% accuracy.

The main weakness is resolution which in the FT  $\propto \frac{1}{\delta_{\max}}$  where  $\delta_{\max}$  is the maximum path difference at recombination. In the static design this depends only on tilt of the mirror. This can be seen from figure 1.0.2 where the path displacement  $\delta_{x'}$  at particular location  $x'$  along the beam width is  $\propto x'$ . If we then let  $x$  denote the lateral position along the linear array then the right side shows that also  $x \propto x'$ . Combining these two then gives  $x \propto \delta_{x'}$ . In words the position on the linear array is proportional to path displacement, which is convenient regarding measurement, but tilting the array cannot contribute to the maximum path difference (everything was set prior to the beamsplitter).

Intuitively these mirrors are very small and tilt cannot achieve the path difference possible with a linear actuator. In addition, the exaggerated angles in figure 1.0.2 show an asymmetry introduced at recombination that gets worse if this is pushed. It's also very difficult to directly quantify the path difference as Aryamana-Mugisha and Williams point out "the accurate measurement of mirror tilt, and hence path difference, is very difficult... because the mirror is positioned by screws rather than micrometers" [1]. Some of the designs mentioned above are able to circumvent this estimation issue by the properties of the optics. Padgett and Harvey estimate  $200 \text{ cm}^{-1}$  for wavelengths above  $300 \text{ nm}$  based on the properties of Wollaston prisms (where the maximum path differences increases

with wave length), and Zhan arrives at  $329\text{ cm}^{-1}$  by relating path difference to the focal lengths of the spherical reflectors used in his Sagnac interferometer [5, 8]. These estimates are typical, and Courtial et al. have embraced this by optimizing their application (UV gas detection) accordingly "sulfur dioxide has a pronounced line structure with a spacing of approximately  $400\text{ cm}^{-1}$  that differentiates it from hydrogen sulfide" [6, 9]. In the research here we follow Aryamanya and Williams suggestion and perform calibrations and estimate resolution by making comparisons with known spectra [1].

In light of this discussion, the five main goals of this research have been to:

- i) Construct the static Fourier transform spectrometer, partially depicted in figure 1.0.2, from optical components and document the process step by step
- ii) Provide a complete overview of FT mathematics through measure theory and functional analysis, as is necessary to rigorously handle the spectroscopy performed with this device
- iii) Provide a complete map and analysis of the processing techniques used, from signal to spectra, in implementing the FT
- iv) Fourier transform interferograms measured with the spectrometer and analyze the results
- v) Investigate the potential for data-mining the new sets of data, quantify the results, and develop methods for assigning statistical significance to the results

Each of these topics has been given its own independent section below. The interferometer was successfully built eight times. Measurements were made with each build and cumulatively 87 interferograms were recorded from H, Hg, Na discharge lamps, a Sylvania lightbulb, and a HeNe laser. This follows suit as: Aryamana and Williams published spectral results for a tungsten-halogen source and didymium filter, Courtial et al. for  $\text{H}_2\text{S}$  and  $\text{SO}_2$ , Padgett and Harvey for a metal halide street lamp, Patterson et al. for Ne and Na discharge lamps, Shardt et al. for polystyrene, and Zhan for a tungsten wire source and a HeNe laser) [1, 9, 5, 6, 2, 8]. The appendix collectively

contains 12 different graphical representations of each sample's data. Eight of these types explored different settings in processing the FT and the remaining four were used to qualitatively identify trends for data mining.

## 2 Constructing the Interferometer

---

This section is dedicated to the details involved with constructing, aligning, and making measurements with the Michelson interferometer partially depicted in figure 1.0.2. Two separate assemblies are detailed step-by-step: the first mounting optical components on breadboards and the second using magnetic bases. Construction was a process and there was a recurring motif of "cradling into alignment" encountered with the positioning and orientation (tilt) of the optics as well as the production of collimated light.

---

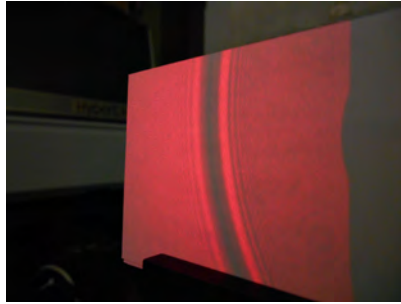
### §2.1 Stage 1: Coarse Positioning and Alignment with HeNe Lasers

---

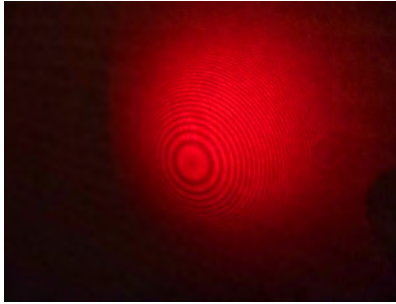
This section covers use of HeNe lasers to coarsely position the interferometer's components and the use of interference patterns in orienting (tilting) optics. The arms of Michelson's interferometer are of equal length and form a right angle. He and Morley made their coarse estimations with a stick [10]. This speaks volumes to the possibilities, and the methodology below simply took advantage of an abundance of HeNe lasers.

Interference was easily produced with the HeNe even repeatedly from drastically misaligned interferometers. But useful patterns for positioning or fine-tuning the locations of the optics were not recognized.

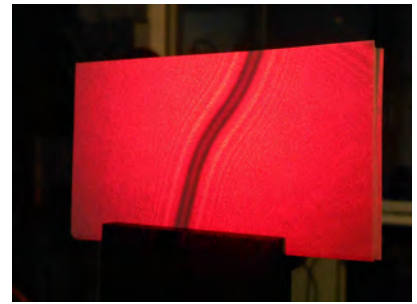




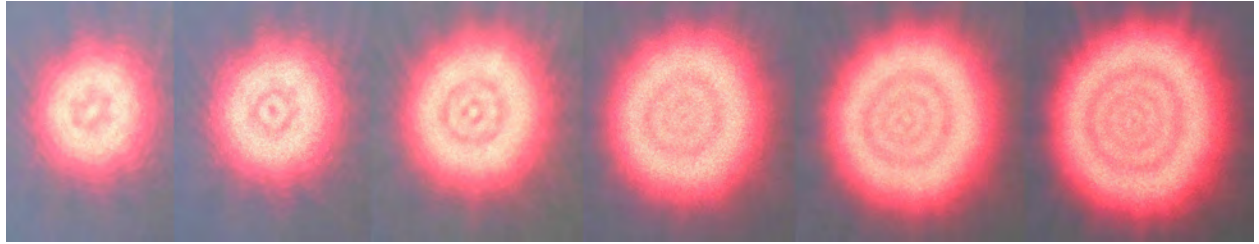
(a) Diffraction with a lens



(b) Magnified interference



(c) Diffraction with a wire



(d) Diffraction with an aperture

Fig. 2.1.1: Examples of HeNe diffraction and interference each easily produced in the lab. On the bottom, an aperture was gradually opened from left to right allowing successive rings to form and the center to alternate between constructive and destructive interference.

However it was found that interference patterns, in general, readily provide information regarding the orientation of optical components.



Fig. 2.1.2: Observed changes in magnified HeNe interference as a reflecting mirror is rotated about its horizontal axis. This rotation produced horizontal fringes and the same naturally held for vertical, diagonal, and arbitrary axes in the optical plane. This behavior was then used to orient optics: coarsely using HeNe interference as shown above (as the magnification introduced dispersion) and then finely with interference from non-coherent sources.

Having ruled out HeNe diffraction and interference as a means to positioning, it was then left to

the straightness of the beam's propagation. This was already being used to align the path along one interferometer arm, and the next advantageous move was to free up the laser's mount.



Fig. 2.1.3: Fastening a HeNe laser to an adjustable mirror mount allowed for greater design flexibility: the design could be changed midstream, the laser repositioned, and the fine adjustments on the mirror mount allowed the beam to produce or be reacquired as a reference line. The single mount was sufficiently stable and an upgrade from the double on the left (shown with an early interferometer design).

This style of mounting was then extrapolated into a two-beam distance replicator and finally a three-beam Predator-Style (PS) System. The PS system both replicated distances and performed linear alignment and this enabled the magnetic base construction detailed in §2.4.



(a) The distance replicator

(b) The PS system

(c) The PS system

Fig. 2.1.4: The distance replicator and PS system. The two beams of the distance replicator were made to intersect at a specific point. This was visible on the faces of optical components and mounts and could be made more sensitive by adjusting the lateral positions of the lasers (shown at a maximum here). Loosening the center screw allowed the apparatus to be rotated and the magnetic base allowed repositioning. Measurements were easily repeated and showed excellent consistency. The lowered lateral bar allowed the a third beam of the PS system to to pass through at optical height for simultaneously linear alignments.

At this point the optical components of the interferometer were positioned as described at the outset by using the PS system to mimic compass and straight-edge construction of the distances and angles.

This procedure is detailed in the beginning portion of §2.4. The mirrors and beamsplitter were also coarsely oriented noting magnified HeNe interference patterns (interference of the beam itself was not large enough to observe) as described in figure 2.1.2. The present alignment was insufficient enough to produce interference from non-coherent sources, which brings us to the next stage.

---

## §2.2 Stage 2: Vibrations, Collimation, and Progressively Finer Alignments

---

At this point there was a Michelson interferometer coarsely aligned by a system of HeNe lasers. With non-coherent sources, if any of the three factors

- vibrational control
- collimation of non-coherent sources
- precision alignment (enough to observe interference from non-coherent sources)

aren't handled correctly then no interference is observed- making things tricky to diagnose.

---

### Vibrations

---

In discussing difficulties with their own apparatus, Michelson and Morley state "...another was its extreme sensitiveness to vibration. This was so great that it was impossible to see the interference fringes except at brief intervals when working in the city, even at two o'clock in the morning." Hence the mercury bath.

The first measure taken here was exchanging the "magnetically aided" optical mounts shown in figure 2.1.3 for the stronger magnetic bases shown in figure 2.1.4. Numerous attempts at incorporating material such as styrofoam and metal slabs into the foundations proved insufficient (even for a glance of interference), and the issue was only resolved after moving to a floating laser table.

At the same time a collimated non-coherent light source had not yet been produced and the issue of vibration was never revisited thereafter. Therefore, as stated in the introduction, it's difficult to diagnose what the problem actually was.

---

## Collimation

---

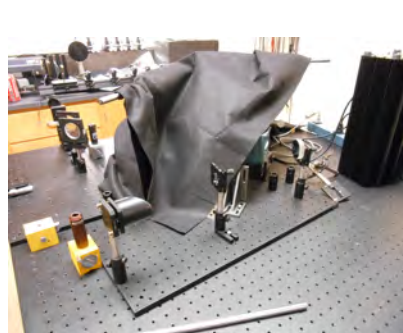
Collimation was a big issue because the interferometer requires straight paths and the non-coherent sources were discharge lamps and a lightbulb. Apertures were used as a first measure and the overall design played off an available parabolic mirror: mirrors avoid chromatic aberration and the paraboloid shape reflects light passing through its focal point into parallel rays (hence no spherical aberration either).



(a) The collimator with a discharge lamp



(b) The aperture used with the lightbulb



(c) The collimator with the lightbulb

Fig. 2.2.1: A horizontal slit initially cut a portion of the source and this was reflected obliquely to evade spillover. A converging lens then attempted to focus the light at the focal point of the parabolic mirror in order to produce a collimated reflection.

The clipping mirror and the paraboloid were given maximum separation to select collimation. Attempts at coarse alignments (orientations and heights) using the HeNe proved insignificant on account of the curvature of the lens and parabolic and HeNe's small beam width. Fixed supports allowed consistent placement of the discharge lamps and this enabled a rough vertical positioning of the optical components. On the paraboloid this was fixed with a collar to allow further adjustments via rotation and the lens was left free to move about the breadboard with its height fixed. Therefore at this point the collimator could be adjusted by

- Rotating the paraboloid

- Adjusting the orientation of the paraboloid
- Changing the position of the converging lens on the breadboard
- Adjusting the orientation of the converging lens

In the dark, the resulting reflection off the parabolic was visible on a business card. Coarse alignment involved optimizing consistency in the width and shape of this reflected beam as the distance of the card varied. A more precise alignment then placed a cross-hairs near the start of the reflected beam's path and attempted to optimize the resolution of its shadow. The idea is that a shadow that remains clearly resolved over distance suggests parallel trajectories and a well collimated beam.

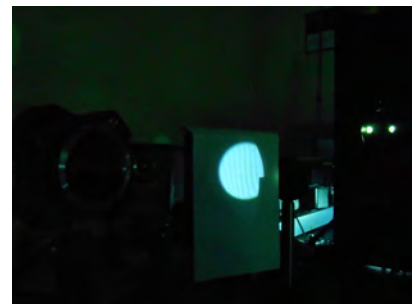
Success was determined by the appearance of interference patterns on an existing student model interferometer. This was crucial in removing collimation from the diagnosis pool as discussed at the beginning of this section. If the end result was insufficient in any way the entire process was reiterated.



(a) Observing the cross-hair's shadow



(b) Passing through a student model interferometer



(c) A successfully collimated Hg lamp

Fig. 2.2.2: Aligning the collimator.

On account of the large number of degrees of freedom with adjusting the collimator, a succinct procedure was never realized and this remained the most tedious and iterative aspect of the entire construction. Consequently the collimator was always constructed on a separate, portable, breadboard that could be placed and rotated to wherever a collimated beam was needed.



## Progressively Finer Alignments and Summary

---

The full details of the remaining alignments are given in the construction sections below. One interferometer mirror was placed on a coarsely adjustable stage and the other on a precision. Progressive alignment began with the most coherent lamp, Na, then moved to Hg and finally the lightbulb (sometimes just the latter two with a bit of luck). The single coarse stage was sufficient for observing Na and Hg but white light interference required the precision.

As discussed at the outset, improper handling of any of the three factors discussed throughout this section result in the lack of an interference pattern. The particular solutions encountered here were highly circumstantial but sufficient for allowing construction.

---

## §2.3 Construction: Step-by-Step Using Breadboards

---

The benefits to breadboard construction were that the prefabricated layout allowed for easy positioning, and the interferometer was portable once it was built. Similarly only the single mounted adjustable HeNe from the full PS system (fig. 2.1.4) was needed for construction, and for brevity we'll simply refer to this as the HeNe. Naturally the downside to breadboards was the sacrifices in design flexibility and sizing. An aperture with a fixed collar on its post was used throughout the construction process and effectively determined the optical height. For brevity we'll refer to this as the fixed aperture (FA), and we'll refer to the post holders simply as holds.

To start, three holds were fastened to the board: one each for the compensator and beamsplitter and another to align the HeNe. Posts were always fastened temporarily within holds prior to tightening, such that their bottom protrusion into the breadboard aided centering, and then removed. Magnetic bases were then placed around the breadboard's perimeter to hold its place (see fig.2.3.2), and the FA and was alternated amongst the tightened holds to align the path of the HeNe.

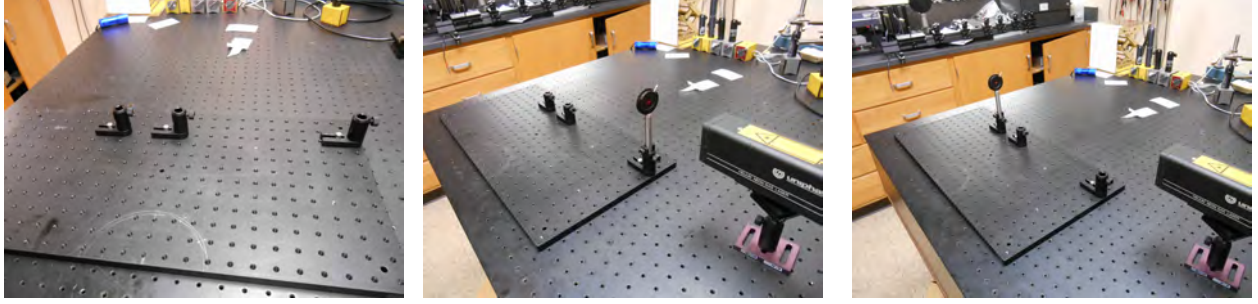


Fig. 2.3.1: The holds from left to right were for: the compensator, the beamsplitter, and to aid HeNe alignment. The two photos on the right show the FA being used to align the path of the HeNe. Magnetic bases (not shown) were used to hold the place of the breadboard as in figure 2.3.2.

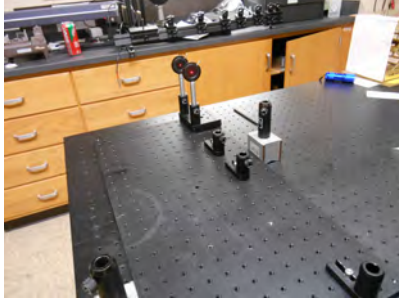
Next the precision stage was installed<sup>1</sup> using 2 holds to align its motion with the HeNe. Positioning was restricted by the breadboard, however the only requirements were:

- That the stages movement be parallel to the HeNe beam
- That the optic would cover the practical beam width encountered when using the interferometer

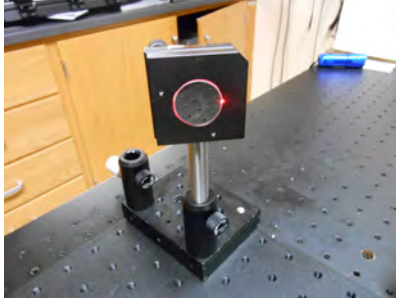
The stage was designed for breadboards and this, along with carefully observed tightening, took care of the former. This left little freedom to address the latter, aside from selecting which portion of the stage to use, but the mirror was indeed large enough that reflecting the practical beam width didn't require exact centering.

An interferometer mirror was then installed on the stage and given coarse vertically centering by observing the HeNe reflect off its ground edge (as above, the mirror was large enough for this centering not to be exact). Once centered vertically, the orientation of the mirror was then adjusted to reflect the HeNe back through the FA.

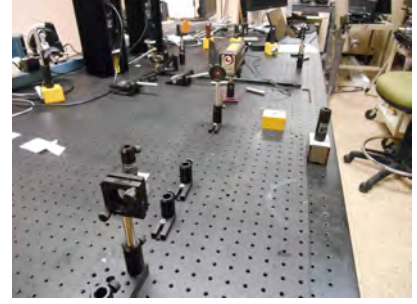
<sup>1</sup>It was important to center the stages prior to installation so that their full range of motion could be used later on.



(a) Aligning the precision stage



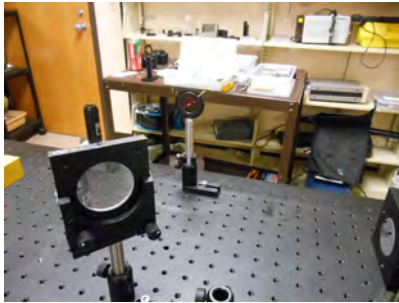
(b) Vertical positioning of the mirror



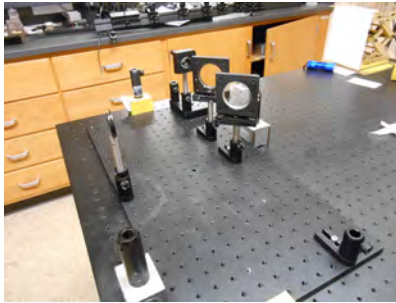
(c) Orienting the mirror

Fig. 2.3.2: Installation and alignment of the first interferometer mirror on the precision stage. Vertical centering is aided by turning the mirror to allow reflection of the ground edge. Orientation was then adjusted by reflecting the HeNe through the FA.

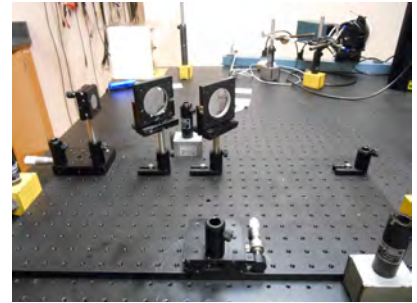
The beamsplitter was then installed. Treating it as a mirror reflecting back to the source, it was centered vertically and oriented using the same procedure as above. It was then rotated to target the FA at a hold installed temporarily to mimic the position of the second interferometer mirror. The compensator didn't significantly affect the beam trajectory and consequently its installation was simply estimated visually (see fig.2.5.3). Following this, the coarse stage was installed at the location of the second mirror.



(a) Rotating the beamsplitter



(b) Visually placing the compensator



(c) The coarse stage

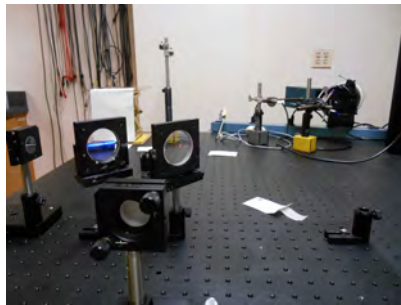
Fig. 2.3.3: The beamsplitter was first aligned as a reflecting mirror and then rotated to target the FA placed in a temporary hold mimicking the location of the second mirror. The reflecting surface on the beamsplitter was opposite to that of the incoming light, therefore the compensator is located directly behind it on the unreflected path.

Installation was then completed by aligning the second mirror on the coarse stage. Vertical centering was performed as with the first mirror. With both interferometer arms operational each mirror was outputting a reflected beam that was clearly visible on the wall. Keeping everything else fixed, the



orientation of the second mirror was then coarsely adjusted to make these beams coincide. The resulting recombined beam was then magnified, causing the interference pattern to be projected on the wall, and the second mirror's orientation was finely adjusted to maximize the resulting centerburst. This last step and the rest of the alignments below were performed with the lights out.

At this point all that remained was to adjust the mirrors' distances to the beamsplitter via the stages. The collimator was positioned to send light through the interferometer and these last alignments were made using increasingly non-coherent sources: first Na, then Hg, then the lightbulb (or just the latter two with care and luck). With the former two, the coarse stage was adjusted to determine a range over which interference was observed or had the most contrast. Its final position was then placed at the median. The lightbulb was treated similarly excepting that only the precision stage was moved (and moved more gently).<sup>1</sup> After practice and with the collimator already built, this entire construction was completed in roughly 30 minutes. The same was true regarding the magnetic base construction, to which we now turn.



(a) Coarsely orienting the second mirror



(b) Finely orienting the second mirror



(c) Interference of the light bulb

Fig. 2.3.4: The final alignments involved coarse and fine adjustments to the orientation of the second mirror, and then adjusting the stages to maximize the intensities of interference patterns created with increasingly non-coherent sources. The point of zero path difference was identified by the appearance of White light interference.

<sup>1</sup> In each construction, it always seemed that after aligning the coarse stage, a first guess at backing out the precision produced interference from the lightbulb. It seemed strange for this to be systematic.

---

## §2.4 Construction: Step-by-Step Using Magnetic Bases

---

The benefits of magnetic base construction were an increased flexibility with design and sizing. This was particularly valuable in the developmental stages and also allowed larger, more accurate, interferometers to be constructed. The trade-off is that without fabricated holes, positioning required using the PS system (fig. 2.1.4). As in the breadboard construction, an aperture with a fixed collar on its post was used throughout the construction process and effectively determined the optical height of the interferometer. For brevity we'll refer to this as the fixed aperture (FA) and we'll refer to the post holders mounted on their magnetic base simply as holds. Similarly we'll refer to the single mounted adjustable HeNe of the PS system simply as the HeNe, and we'll denote the distance replicating portion of the PS system as DR.

To start, two holds were anchored at the desired distance for the interferometer arm. The FA was then alternated between the holds to align the path of the HeNe.

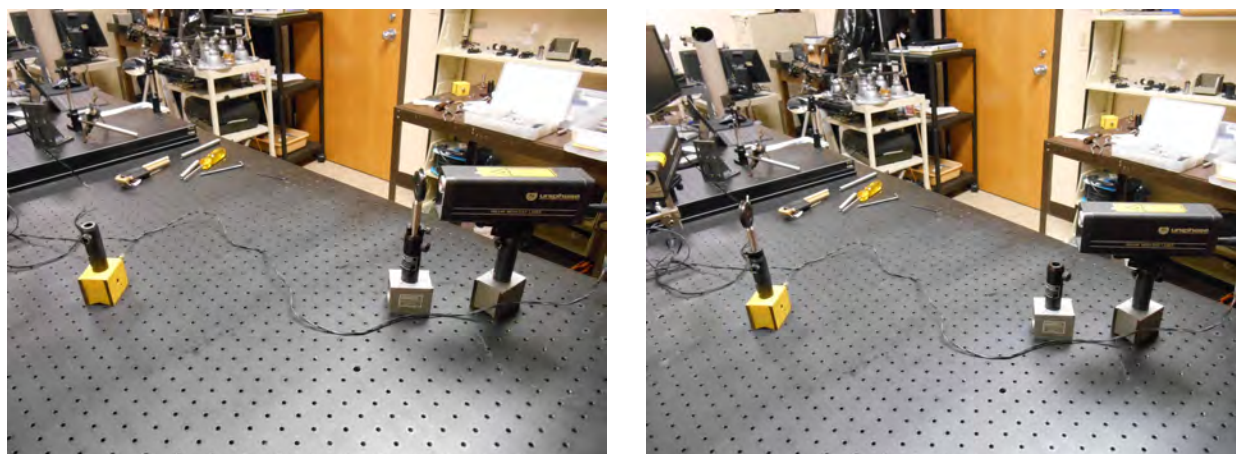


Fig. 2.4.1: The hold on the left was for the beamsplitter while the right would support an interferometer mirror. The FA was alternated to align the HeNe. An orientation askew to the laser table was chosen to emphasize the independence of this construction of the prefabricated holes.

The DR was then placed in the beamsplitter's hold and was aligned with the FA to replicate the distance of the interferometer's arm. By rotating the DR and using the HeNe's beam, a third hold

was then placed opposite the first such that both were equidistant to the beamsplitter's hold.<sup>1</sup> The distancing was then confirmed with repeated measurements made by rotating the DR.

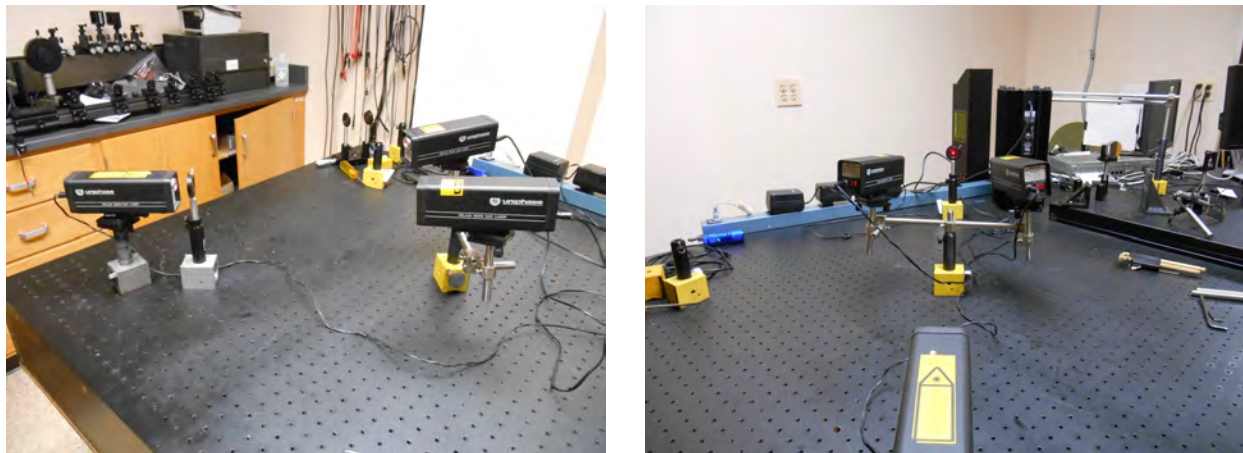


Fig. 2.4.2: Replicating the distance between the two holds, a third was then placed in line with the first two.

The next steps simply emulated compass and straight edge construction in order to make the interferometer arms perpendicular. The DR was placed in one of the exterior holds and adjusted to the largest distance afforded by the table. The DR was then alternated between the exterior holds, and a fourth hold was eased into a position that was equidistant from both: effectively producing a right angle to the HeNe's beam.

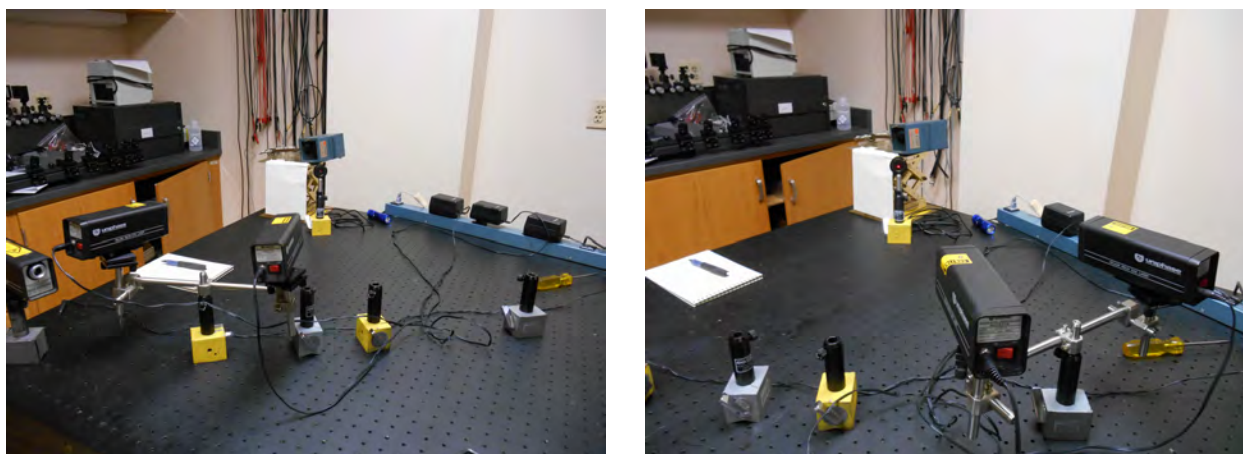


Fig. 2.4.3: Emulating compass and straight edge construction, the DR was used to produce a right angle. The set up here is from a previous construction.

<sup>1</sup>When using the DR it was important to consistently use the same side of the same aperture.



The HeNe was then moved and realigned, again by alternating the FA, to produce a beam perpendicular to its original path.

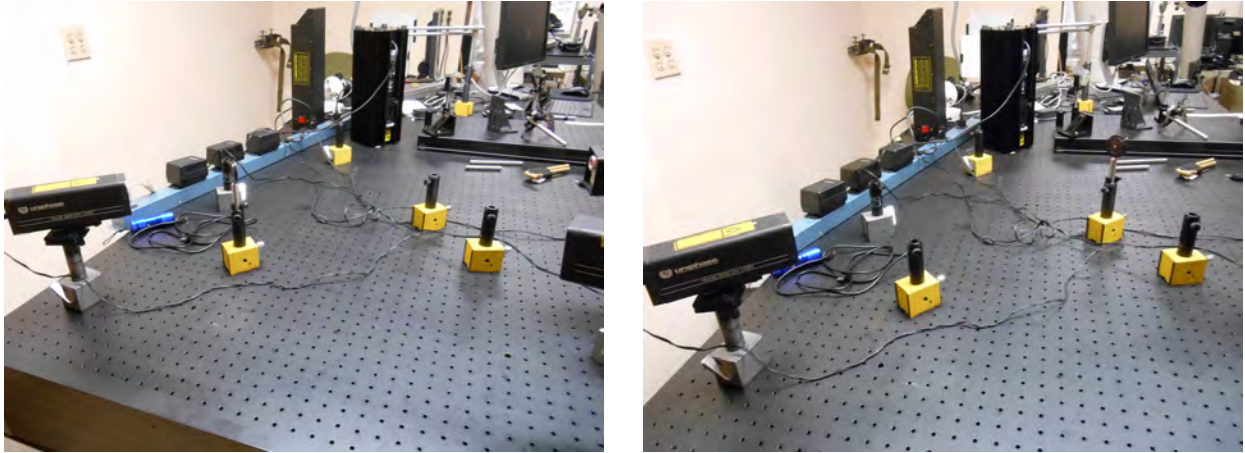


Fig. 2.4.4: Aligning the HeNe perpendicular to its original path by alternating the FA.

The realigned HeNe and the DR were then used to position and align the precision stage. Two apertures were mounted on the stage in order to align its movement with the HeNe and the stage was eased into such a position at equidistance marked by the DR.



Fig. 2.4.5: Alignment of the precision stage with the PS system. After alignment, the DR was then rotated to the other two exterior holds to verify the measurement is consistent.

As the coarse stage would be placed on the hold from the first step, at this point the layout was complete. An interferometer mirror was then installed on the precision stage, and was vertically aligned and oriented via reflection through the FA as depicted in figure 2.3.2. The beamsplitter was installed and oriented by treating it as a mirror and using the same process. Once this

was completed it was rotated to target the FA in the hold from the first step (where the second interferometer mirror would be). The compensator was vertically aligned in the same way but, as it was not observed to alter the beam path, was aligned by sight.

Keeping its magnetic base fixed, post holder on the first hold was removed and replaced by the coarse stage.<sup>1</sup> The second mirror was then installed on the coarse stage and vertically centered by the same procedure above. At this point the remainder of the procedure, orienting the second mirror and making precision alignments with the stages, was exactly the same as with the breadboard construction. This is detailed in the last two paragraphs of the previous section so we'll just jump to the end result here.

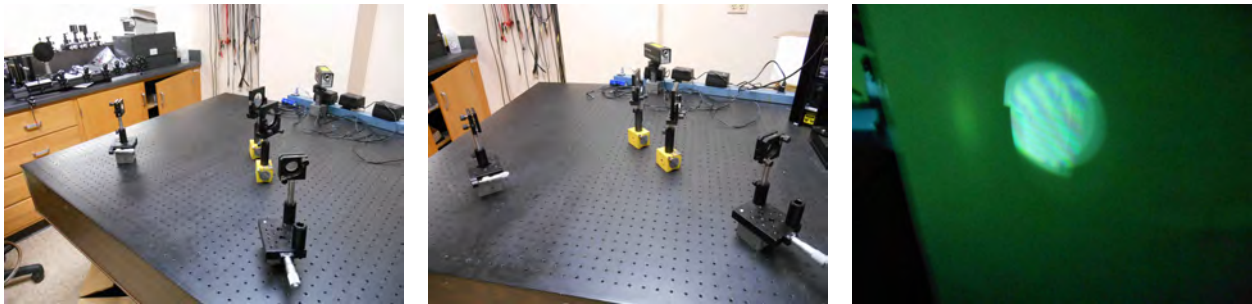


Fig. 2.4.6: The complete construction was elegantly comprised of only four pieces (shown from two perspectives). The right shows the resulting Hg interference.

---

## §2.5 Parts Used in Constructing the Interferometer

---

This section provides information regarding the mirrors, beamsplitter, compensator, and stages used in the constructions above. The linear array CCD detector used to measure the interferograms is discussed in the following section.

The interferometer mirrors (Thorlabs PF10-03-G01) were 25.4 mm protected aluminum with  $> 90\%$  average reflectance from  $450\text{ nm} - 2\text{ }\mu\text{m}$  and  $\lambda/10$  flatness at  $632.8\text{ nm}$ . The beamsplitter (Thorlabs

---

<sup>1</sup>This was not done initially because the coarse stage would have altered the height of the DR.

BSW27) was  $50.8 \times 8$  mm UV fused silica with  $\lambda/2$  flatness at 633nm and was specified for a range of 350 – 1100 nm.

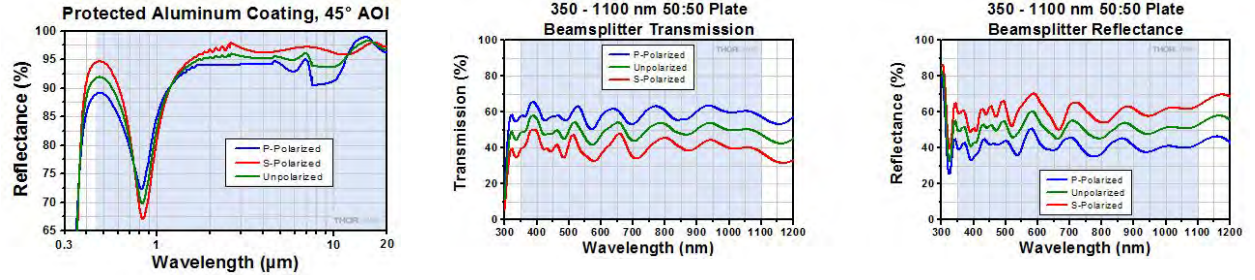


Fig. 2.5.1: Manufacturer's specifications for the reflectance and transmittance of the mirrors and beamsplitter.

A compensator is also required because one path necessarily traverses the beamsplitter more than the other.

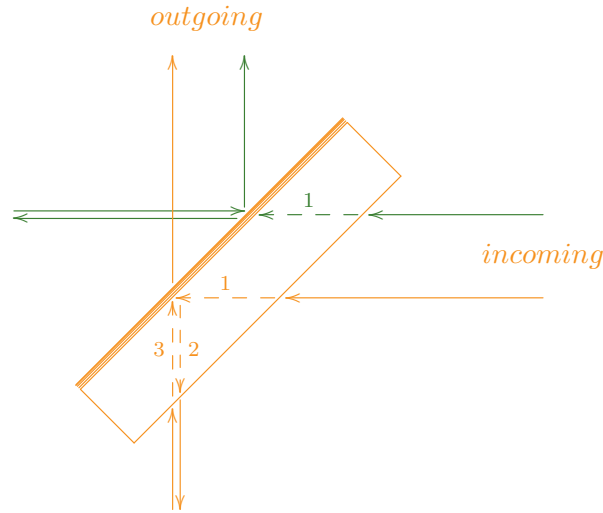


Fig. 2.5.2: To split the beam, one side of the beam splitter is given a partially reflected coating (shown in bold). Transmitted (green) and reflected (orange) light then pass through once and three times, respectively. To make this more even, a compensator made of the same material and thickness is placed in the arm of the interferometer of the transmitted beam to introduce two more passages.

Without a compensator, interference was observed (not measured) only once with Na and Hg, but this was never reproduced. However the compensator is, relatively, very flexible. Thorlabs does not manufacture a compensator for the BSW27, and it was sheer luck that happened upon a window

appearing to be of similar composition (fused silica).<sup>1</sup>

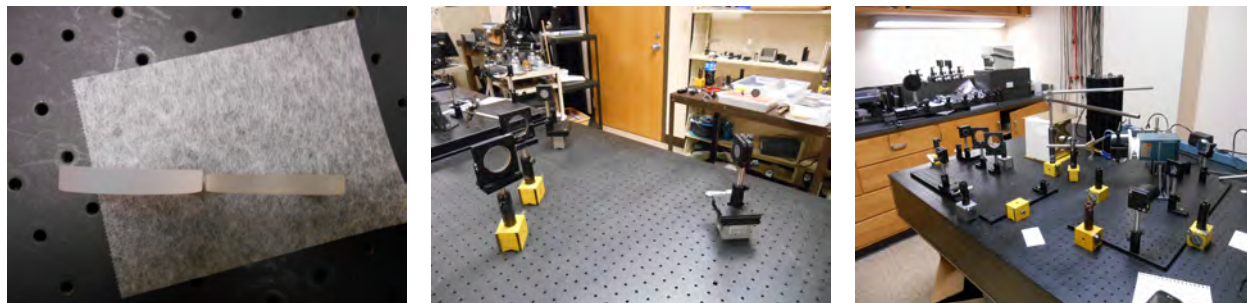


Fig. 2.5.3: The beamsplitter (left) was slightly thicker than the compensator but this did not hinder the production of interference. The center shows the beamsplitter (foremost) with the compensator placed directly behind in the path of the transmitted beam. This is shown again on the right along with the collimator producing the incoming beam.

Along with the leeway in thickness, there was also reasonable flexibility in positioning and orientating the compensator. Precise orientation and positioning wasn't possible as the compensator had no perceptible effect on the path of the HeNe, and these were simply estimated visually. After interference was established, it was possible to rotate the compensator and, except at the more extreme angles, still observe an interference pattern.

Finally, the coarse stage was a Newport Model 420 and the precision was something manufactured by Thorlabs (PT1?; see Dr. Landahl). Interferometers constructed with just the Newport were sufficient for producing interference with Na and Hg, but white light interference absolutely required the precision stage.

---

<sup>1</sup>All attempts with other materials failed.

---

## §2.6 Measurements: The Instrument, Settings, and Labeling Samples

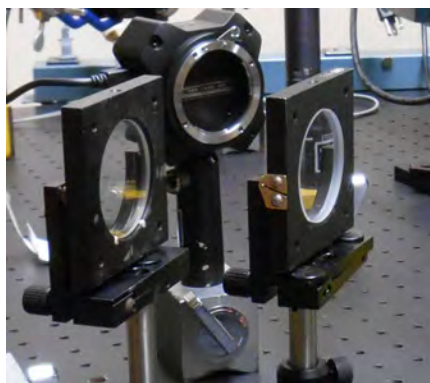
---

Interferograms were sampled with a Thorlabs LC100 linear array detector. The array consisted of 2048 CCDs,  $14 \times 56 \mu\text{m}$  with  $14 \mu\text{m}$  pitch (the CCDs are virtually adjacent), and Thorlabs specifies a detector range of 350 – 1100 nm. The intensity of each CCD was measured at 5 ms intervals for roughly 500 ms and output to CSV files via USB and Thorlabs *Spicco* software.

Initially data was collected over 1000 time intervals and these few samples gave promising results for a unique kind of data mining (see **Fig.??**). However without knowing this the method was reduced to 100 time intervals on account of producing sluggish .csv's. The time stamps recorded from the LC100 showed tended to vary  $\pm 1$  ms from a regular 5 ms output.

The interferometer was successfully built eight times. Measurements were made with each build and cumulatively 87 interferograms were recorded from H, Hg, Na discharge lamps, a Sylvania lightbulb, and a HeNe laser. (along with 25 background measurements).

- HeNe [Uniphase 1508-0] (4 samples)
- H arc lamp [VWR 470014-474] (4 samples)
- Hg arc lamp [Pasco] (27 samples)
- Na arc lamp [Pasco] (24 samples)
- Sylvania 60 W clear lightbulb (28 samples)



In all cases alignment had successfully produced white light interference prior to measuring samples. Excepting H on account of its low intensity at recombination, interference patterns were always visible at the time of measurement.

Fig. 2.6.1: The LC100 shown mounted behind



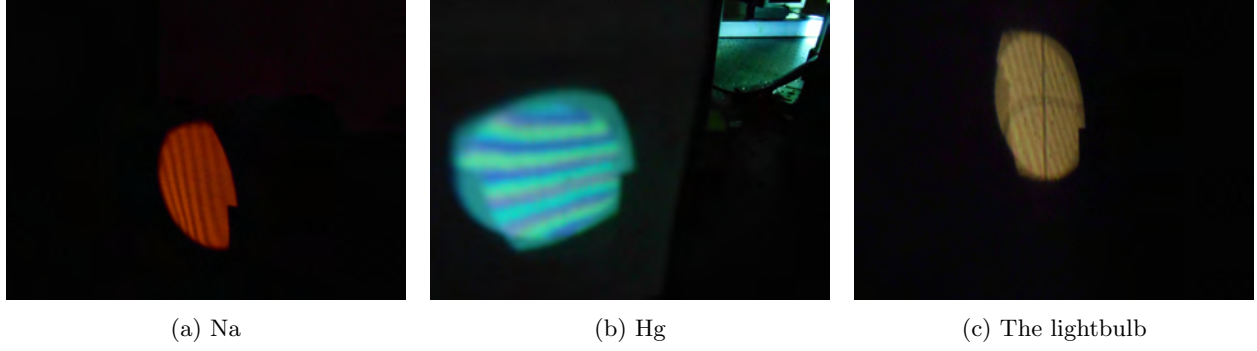


Fig. 2.6.2: Observed interference patterns. The interference from H was not visible on account of the low intensity at recombination but the expected pattern was measured with the LC100 (see fig.4.1.1).

Measured samples were labeled with serial numbers that indicate type of sample, the build of interferometer being used, and then by the timestamp<sup>1</sup>

year	month	day	build	minute	second
##	##	##	#	####	##

of their original recording. Interferometers were rebuilt (at least) each day so the day and build number together uniquely identify the interferometer that was used.

Misalignments were introduced to some measurements with the intent of data mining for information that would later be useful in aligning the interferometer. Such samples were labeled with the terms *horizontal* and *vertical* to indicate the fringe direction of the resulting interference pattern upon misalignment. The symbols < and > were then appended to indicate if this was to a lesser or greater extent, respectively.

From here the measurements moved on to data processing which is detailed in the remaining sections and the appendix.

---

<sup>1</sup> The times of measurement were conveniently retrieved from the .csv files' metadata.

### 3 Fourier Transform Mathematics

---

This section provides an overview of Fourier transform mathematics through measure theory and functional analysis. The purpose of this treatment is to:

- i) Describe under what cases the inverse transformation will reproduce an original function: physically, in what cases will the combination of frequencies indicated by the transform reproduce the original signal we measured.
- ii) Work within a consistent framework in order to:
  - Get expected FT results from transforming simple things like the sine function
  - Perform transforms with useful expressions like Dirac's delta
  - Be able to perform derivations regarding the resolution of the instrument

These are elaborated with the discussion of the physical interpretation in the following section. The measure-theoretic results take the first steps to treating i). In addition, this also expands the class of functions we can integrate (hence transform) from Riemann to Lebesgue, and Plancherel's transformation gives us the first example of the FT being *extended*. Functional analysis then provides the extension we need to finish the rest of the goals above. All of the mathematical results, excepting §3.1, §3.7, and §3.8, have been cited exclusively from Walter Rudin [11],[12].

It's unreasonable to provide complete derivations of the more advanced treatments. In lieu, §3.2-§3.4 provide a fast paced references to the definitions and background necessary to understand the language with which the FT results are stated. These are by no means computationally heavy but the difficulty rather lies in the *abstractness*. As Rudin explains [11]:

*It seems that the relations between these concepts emerge most clearly when the setting is quite*

*abstract, and this (rather than a desire for more generality) motivates our approach to the subject.*

In short, we can see the forest through the trees.

---

## §3.1 The Physical Interpretation

---

The initial idea and physical interpretation of Fourier transforms in spectroscopy is simple: we want to decompose a signal into constituent frequencies such the original signal is the sum of these parts. Conversely, the sample we're measuring only allows certain electron energy transitions, and we assume that our signal results from the sum of such transitions.

The FT is associated with signal decomposition and is defined in the calculus setting as

**Definition 3.1.1.** *Given a complex function  $f$  defined on  $\mathbf{R}$ , its Fourier transform  $\hat{f}$  is defined as*

$$\hat{f}(t) = \int_{-\infty}^{\infty} f(x)e^{-ixt}dm(x)$$

*The Fourier transform is also used to refer to the map  $f \mapsto \hat{f}$ .*

while the inverse transform shows the signal reconstituted

**Definition 3.1.2.** *Given a complex function  $\hat{f}$  defined on  $\mathbf{R}$ , its inverse Fourier transform  $g$  is defined as*

$$g(x) = \int_{-\infty}^{\infty} \hat{f}(t)e^{ixt}dm(t)$$

Some disconnects between our physical situation and this mathematical representation can be acknowledged immediately.

- i) As we understand them, particles are *countable*.<sup>1</sup> Therefore assuming each photon originates from a transition in the measured sample, there are not enough electrons in the universe to produce the smallest interval of continuous frequencies  $t$ . Therefore what the transform is creating mathematically, and what the inverse is implying, are in discord with some very fundamental scientific understandings.
- ii) This representation innately assumes that the contribution of any frequency manifests in the form of a trigonometric function which, excepting cases involving the simplest potentials, doesn't seem reasonable.

We can try to evade i) by using a Fourier Series, but the results in 3.5.3 show that this also introduces severe inconsistencies. Moving on, we can look at some problems that arise with approaching the FT with calculus and with the FT definitions above.

- Physically we want the inverse transform to reproduce our original function. This is not true in general, as we'll see below, but calculus certainly isn't well equipped for making this determination.
- In accordance with our physical interpretation, a sine function should represent light comprised of a single frequency. We know what the transform should be, but using  $f(x) = \sin(x)$  in the definition above gives an integrand that isn't Riemann (or Lebesgue) integrable.
- Simple and useful ideas that have become standard practice with the transform aren't given consistent explanations with calculus.
  - The sinc function is the FT of the box function and these are useful, amongst other things, in interpreting the resolution of an FT spectrometer. The integral of sinc converges but not absolutely, and the same is true for the product  $\text{sinc} \cdot e^{-ixt}$  as can be seen from

$$\int_{(n-1)\pi}^{n\pi} \frac{|\sin(x) \sin(xt)|}{x} dx \geq \frac{1}{n\pi} \left| \int_{(n-1)\pi}^{n\pi} \sin(x) \sin(xt) dx \right| = \frac{k}{n}$$

---

<sup>1</sup>A set  $S$  is *countable* if there exists an injection from  $S$  to the integers. For the particular claim, fix a particle, a direction, and an enumeration of the rationals  $q_1, q_2, \dots$ . Beginning at a distance of  $q_1$ , begin counting particles heading clockwise from the given direction, then move on to  $q_2$  and so on.

The Riemann rearrangement theorem then tells us that we can rearrange the positive and negative contributions to this integral to produce any value we want. Physically this means that a sinc function could produce any spectra that we wish, or physically that a sinc spectra can produce any signal that we wish, and clearly this needs to be remedied.

- Dirac’s function isn’t Riemann or Lebesgue integrable, so calculus (nor measure theory) can offer a consistent framework for working with it.

Our overall purpose is then to elevate the approach to FTs to measure theory and finally functional analysis in order to remove these deficits as best can be, and in order to gain insight into how our mathematical model interplays with the physical situation described above.

---

## §3.2 Background and Definitions: Topologies and Measure Spaces

---

The definitions provided here and in the next section are fundamental to understanding the language with which the FT results are stated. As definitions they require no proof: they simply have been naturally selected for their utility. It’s easy to look up examples, so we’ll stick to our premeditated abstract route described at the outset.

Let  $X$  be an arbitrary set (numbers, vectors, functions... whatever). A *topology* ( $\tau$ ) and a  $\sigma$ -*algebra* ( $\mathcal{F}$ ) on  $X$  are of collections of subsets of  $X$ .

---

### Topologies and $\sigma$ -Algebras ( $\sigma$ -Fields)

---

**Definition 3.2.1.** A collection of subsets  $\tau$  is a **topology** if:

(i)  $\emptyset, X \in \tau$  (where  $\emptyset$  is the empty subset)

(ii)  $A_i \in \tau$  for  $i = 1, 2, \dots, n \implies \bigcap_{i=1}^n A_i \in \tau$

(iii) If  $\{A_\alpha\}$  is an arbitrary collection of members of  $\tau$ , then  $\bigcup_\alpha A_\alpha \in \tau$

In words, a collection of subsets is a topology if it contains  $\emptyset$ ,  $X$  and is closed under arbitrary unions and finite intersections. A  $\sigma$ -algebra is defined slightly differently:

**Definition 3.2.2.** A collection  $\mathcal{F}$  is a  $\sigma$ -algebra if:

(i)  $X \in \mathcal{F}$

(ii)  $A \in \mathcal{F} \implies A^c \in \mathcal{F}$

(iii)  $A_i \in \mathcal{F} \ \forall i \implies \bigcup_i A_i \in \mathcal{F}$

being closed under compliments and countable<sup>1</sup> unions.<sup>2</sup> The members of a topology are referred to as *open* while those of a  $\sigma$ -algebra are *measurable*. A set  $X$  upon which these structures exist is referred to as a *topological space* and *measurable space*, respectively. We now have established enough to move on to our next two definitions, which bring us most of the way to the Lebesgue integral that forms the basis of the measure theoretic approach.

---

## Measurable Functions

---

**Definition 3.2.3.** Given a measurable space  $X$  and topological space  $Y$ , a function  $f: X \longrightarrow Y$  is **measurable** if  $f^{-1}(A) \in \mathcal{F} \ \forall A \in \tau$ .

The Lebesgue integral will combine the notion of a measurable function with that of a *measure*: which relates only to the  $\sigma$ -algebra.

---

## Measures

<sup>1</sup> A set  $S$  is *countable* if there exists an injection  $\mathbf{Z} \rightarrow S$ .

<sup>2</sup>The difference between *countable* and *arbitrary* is why the index  $\alpha$  was used (iii) of 3.2.1 but we see  $i$  in Definition: Sigma Algebra.

---

**Definition 3.2.4.** Given a  $\sigma$ -algebra  $\mathcal{F}$ , a **measure** is a function  $\mu : \mathcal{F} \longrightarrow [0, \infty]$  such that if  $\{A_i\}$  is a disjoint countable collection of members of  $\mathcal{F}$ , then

$$\mu \left( \bigcup_i^\infty A_i \right) = \sum_{i=1}^\infty \mu(A_i)$$

The last definition of this section plays off this.

---

## Almost Everywhere

---

**Definition 3.2.5.** Let  $\mathcal{F}$  be a  $\sigma$ -algebra on a set  $X$  with measure  $\mu$ . A property exists **almost everywhere (a.e.)** in  $X$  if it holds for all  $x \in X$  except perhaps on a set of measure zero.

Notice that, by 3.2.4, a countable union of sets of measure zero is also a set of measure zero. We can now move on to Lebesgue integration.

---

## §3.3 Background and Definitions: Lebesgue Integration and $L^p$ Spaces

---

As with the previous section, the concepts and definitions presented here are fundamental to understanding the language with which the FT results are stated. As definitions they require no proof, and history has chosen to preserve that of the Lebesgue integral because:

- It allows more functions to be integrated (Riemann integrable functions are a subset of Lebesgue integrable)
- It's very well suited to evaluating limits (these tools enable the more complete treatment of the Fourier transform)

The definition is built upon a simple case. For brevity, in the remaining sections we'll assume that:  $X$  is equipped with  $\sigma$ -algebra  $\mathcal{F}$  and measure  $\mu$ , and that the complex field  $\mathbf{C}$  is referenced with its standard topology.

---

## Simple Functions

---

**Definition 3.3.1.** *A simple function  $s: X \rightarrow \mathbf{C}$  has a range consisting of only finitely many points.*

Letting  $\alpha_1, \alpha_2, \dots, \alpha_n$  be the distinct values,  $A_i : \{x : s(x) = \alpha_i\}$ , and  $1_{A_i}$  be the indicator function on  $A_i$ , then a useful expression of simple functions is

$$s = \sum_{i=1}^n \alpha_i 1_{A_i}$$

By 3.2.3, it's easily seen that  $s$  is measurable *iff*  $A_i \in \mathcal{F} \forall i$ . Our founding definition of integration also follows readily.

---

## Integrals of Simple Functions

---

**Definition 3.3.2.** *Let  $s : X \rightarrow [0, \infty)$  be a simple measurable function and let  $E \in \mathcal{F}$ . Then we define*

$$\int_E s \, d\mu = \sum_{i=1}^n \alpha_i \mu(A_i \cap E)$$

We'll fully extrapolate this in two steps.



---

## Integrals of Non-Negative Functions

---

**Definition 3.3.3.** If  $f: X \rightarrow [0, \infty]$  is measurable, then we define

$$\int_E f \, d\mu = \sup \int_E s \, d\mu$$

where the supremum is taken over all simple measurable functions  $s: X \rightarrow [0, \infty)$  such that  $0 \leq s \leq f$ .

---

## Integrals of Complex Functions

---

Our final step is to generalize to this to complex measurable functions  $f$ . As projections are continuous<sup>1</sup>, the real ( $u$ ) and complex ( $v$ ) parts of  $f$  are also measurable (3.2.3). A separate argument then shows that  $u^+ = \max\{u, 0\}$  and  $u^- = -\min\{u, 0\}$  (and similarly for  $v$ ).<sup>2</sup> As each of these components is positive, and therefore integral by 3.3.1, we can then define

**Definition 3.3.4.** Letting  $f: X \rightarrow \mathbf{C}$  be measurable with real part  $u$  and complex part  $v$ , then  $f = u^+ - u^- + iv^+ - iv^-$  and we can define

$$\int_E f \, d\mu = \int_E u^+ \, d\mu - \int_E u^- \, d\mu + i \int_E v^+ \, d\mu - i \int_E v^- \, d\mu$$

provided that at least one out of each max/min pair is finite.

This completes the definition of the Lebesgue integral and, as in the previous section, we'll again close with something used explicitly in the Fourier results.

---

<sup>1</sup>Equipping  $X$  and  $Y$  with topologies  $\tau_X$  and  $\tau_Y$ , respectively, a function  $g: X \rightarrow Y$  is **continuous** iff  $g^{-1}(A) \in \tau_X$  for all  $A \in \tau_Y$ .

<sup>2</sup>Here  $u$  can be any measurable function.

---

## $L^p$ Norms

---

**Definition 3.3.5.** Letting  $0 < p < \infty$ , the  $L^p(\mu)$  norm of a measurable function  $f$  is defined as

$$\|f\|_p = \left\{ \int_X \|f\|^p d\mu \right\}^{1/p}$$

The set of all functions such that  $\|f\|_p < \infty$  is denoted  $L^p(\mu)$ .

There are two important points to keep in mind. The content of the first is common but beyond our scope to derive.

- For any such  $p$ ,  $L^p(\mu)$  is a Banach space (thus a vector space). The cases of  $p = 1, 2$  will be relevant to our Fourier results below, and  $L^2(\mu)$  in particular has the additional structure of a Hilbert space.
- It can be shown using 3.3.2 that the integral of a function  $f$  is independent of its definition on any set of measure zero: if  $f = g$  a.e. (see 3.2.5), then the integrals of these functions are equal. Therefore when considering  $L^p(\mu)$  it is appropriate to think of a function  $f$  instead as an equivalence class of functions where  $f \sim g$  if  $f = g$  a.e.

Having established Lebesgue integration, our final step before stating the results is introducing Lebesgue measure (deriving its existence is also common but slightly beyond our scope).

---

## §3.4 Background and Definitions: Lebesgue Measure

---

Our final step is to replace our general abstract measure  $\mu$  with the particular Lebesgue measure  $(m)$ , which has definitions on all the Euclidean spaces  $\mathbf{R}^n$ . This is the standard measure that gives

the results you'd expect when integrating. It's existence is undoubtedly plausible but just enough beyond our scope to be stated without proof here (several derivations exist)

**Theorem 3.4.1.** *There exists a positive complete measure, known as the **Lebesgue measure**  $m$ , defined on a  $\sigma$ -algebra  $\mathcal{F}$  in  $\mathbf{R}$  such that  $m(a, b) = |a - b|$  for all intervals  $(a, b)$  and  $[a, b]$ .*

The term *complete* indicates that any subset of measure zero is also of measure zero. The Lebesgue measure is a *Borel* measure- meaning the  $\sigma$ -algebra  $\mathcal{F}$  on which it is defined contains all open sets (and, of course, their compliments) in the standard topology on  $\mathbf{R}$ . Therefore  $\mathcal{F}$  contains all sets of the forms

$$\bigcup_{\alpha} (a_{\alpha}, b_{\alpha}) \qquad \bigcap_{\alpha} [a_{\alpha}, b_{\alpha}]$$

where  $\alpha$  may range over any index set (the former expression above encompasses all open sets).<sup>1</sup>

At this point we can give a small example of how the Lebesgue integral goes beyond the Riemann. Notice that, by 3.4.1,  $m(r) = 0 \ \forall \ r \in \mathbf{R}$  (any singleton set). As  $\mathbf{Q}$  is a countable collection of singletons,  $m(\mathbf{Q}) = 0$  by 3.2.4.<sup>2</sup> By the comments after 3.3.5, any function  $f$  can then be redefined on  $\mathbf{Q}$ , in any imaginable way, without changing its resulting integral. In comparison, testing these kinds of freedoms quickly produces functions for which the Riemann integral doesn't exist.

The other main benefit of the Lebesgue integral is that it lends itself very nicely to evaluating limits. This allows derivations of results that may not be possible with calculus- including our main results here, for which we have now developed enough language to state.

---

## §3.5 Results: from Measure Theory

---

Here we state measure theoretic results regarding the Fourier transform in the language developed over the previous three sections. To ease the notation,  $m$  is used to denote the Lebesgue measure

---

<sup>1</sup>  $\mathcal{F}$  also contains many other sets that may be less intuitive.

<sup>2</sup> Note, with abstraction, the ease of this result.

(§3.4) multiplied by  $1/\sqrt{2\pi}$ .<sup>1</sup> Similarly, the norm  $L^p(m)$  (3.3.5) is shortened to  $L^p$ . For simplicity we can also leave the units of  $t$  undefined until §4.5, but it's easy to see now that evaluating these functions requires they be proportional to the inverse units of  $x$ .

---

## Fourier Transforms in $L^1$

---

To start, note that by 3.3.5 and the definitions of the Fourier transform given in §3.1, if  $f \in L^1$  then  $\hat{f}(t)$  is defined  $\forall t$ . Our first main result, stated without proof, is

**Theorem 3.5.1.** *If  $f \in L^1$  and  $\hat{f} \in L^1$ , and if*

$$g(x) = \int_{-\infty}^{\infty} \hat{f}(t) e^{ixt} dm(t)$$

*then  $g$  is continuous (and vanishes at infinity) and  $f = g$  almost everywhere.*

This takes us part of the way to goal i) from §3.1 if  $f \in L^1$ , but under the condition that we know  $\hat{f} \in L^1$ . Further analysis shows that the Fourier transform maps  $L^1$  into a *proper* subset of  $C_0$ : the set of continuous functions that *vanish at infinity*.<sup>2</sup> As  $C_0$  is, most conservatively, the exact behavior expected from an EM wave- this says that the inverse transform of functions  $\hat{f}(t) \in L^1$  cannot reproduce all the signals we'd expect to measure.

---

## Fourier Transforms in $L^2$ : The Plancherel Transformation

---

Our second result from measure theory gives us the first instance of the Fourier transform defined in §3.1 being *extended* in a logical way. Here the map  $f \longrightarrow \hat{f}$  is an extension of the Fourier transform to a Hilbert space isomorphism on  $L^2$  and is known as the *Plancherel transformation*.

---

<sup>1</sup> 3.2.4 easily verifies that this is indeed a measure.

<sup>2</sup> This is a separate result; one of Rudin's problems.

**Theorem 3.5.2.** *For each  $f \in L^2$  there exists a unique  $\hat{f} \in L^2$  such that the following properties hold:*

- (a) *If  $f \in L^1 \cap L^2$  then  $\hat{f}$  is the previously defined Fourier transform (3.1.1).*
- (b) *For every  $f \in L^2$ ,  $\|f\|_2 = \|\hat{f}\|_2$*
- (c) *The mapping  $f \longrightarrow \hat{f}$  is a Hilbert space isomorphism of  $L^2$  onto  $L^2$ .*
- (d) *The following symmetric relation exists between  $f$  and  $\hat{f}$ : If*

$$\phi_A(t) = \int_{-A}^A f(x)e^{-ixt}dm(x) \quad \text{and} \quad \psi_A(x) = \int_{-A}^A \hat{f}(t)e^{ixt}dm(t)$$

*then  $\|\phi_A - \hat{f}\|_2 \rightarrow 0$  and  $\|\psi_A - f\|_2 \rightarrow 0$  as  $A \rightarrow \infty$ .*

The problem here is that the existence of an isomorphism doesn't guarantee that its inverse transformation is described by 3.1.2. This becomes pronounced in part (d) where, in lieu of the equality a.e. in 3.5.1, we receive convergence without guarantee of rate or monotonicity. A separate result gives the existence of a *subsequence* of  $\psi_A(x)$  that converges to  $f(x)$  a.e. [and similarly for  $\phi_A(t)$ ].<sup>1</sup>

---

## Fourier Series

---

Our last result pertains to the Fourier series.

**Theorem 3.5.3.** *Let  $T \subset \mathbf{R}$  be any closed interval and  $|T|$  be its length. Let  $C(T)$  denote the set of continuous complex functions on  $T$ . If we define the inner-product*

$$\langle f, g \rangle = \frac{1}{|T|} \int_T f(x)\bar{g}(x) dm(t)$$

*and for  $f \in C(T)$  the series*

---

<sup>1</sup> This involves relating  $L^p$  convergence to convergence a.e.

$$\hat{f}(t) = a_0 + \sum_{n=1}^{\infty} c_n e^{int}$$

where  $c_n = \langle f, e^{int} \rangle$ , then there is a dense set of functions in  $C(T)$  for which the  $\hat{f}(t)$  diverges on a dense set of  $T$ .

To elaborate,  $C(T)$  is a complete metric space under the supremum norm

$$\|f\|_{\infty} = \sup\{|f(t)| : t \in T\}$$

For a set  $S \subset C(T)$  to be dense means that for any  $f \in C(T)$  and any  $\epsilon > 0$ , there is a function  $g \in S$  such that  $\|f - g\|_{\infty} = \sup\{|f(t) - g(t)|\} < \epsilon$ . In words, for any such  $f$  there is a function in  $g \in S$  that gets as close to it, uniformly, as we'd like. The theorem then states that not only does the series above diverge on such a set  $S$  but that, for every  $g \in S$ ,  $\hat{g}(t)$  will diverge on a dense set of  $t$  values. Physically this means that if we represent a measured signal in terms as a Fourier series then there is another continuous signal out there, that is as close to the one we measured as we like, for which the Fourier series will diverge on a dense set of frequencies. This other signal would then certainly not be equivalent to the sum of its constituent parts and this is a wild break from our physical interpretation of the FT.

---

## Conclusions

---

Overall these results still leave us short of accomplishing *i)* of §3.1, and we have made no progress towards *ii)*: sine is neither in  $L^1$  nor  $L^2$  unless we restrict the domain as in our last theorem above- and that gives us worse problems. In addition, as the Dirac delta equals zero a.e., any integrals involving it should be zero by §3.3.

However we've been able to answer questions much more thoroughly than with calculus, and these results tell us clearly that there are problems with the mathematical interpretation we've chosen

to represent spectra. Therefore we'll push on to functional analysis.

---

## §3.6 Results: from Functional Analysis

---

This approach first restricts the Fourier transform to  $\mathcal{L}_n$ : the set of *rapidly decreasing functions*. The trick is then to extend this to  $\mathcal{L}_n'$ : the set of continuous linear operators on  $\mathcal{L}_n$ , known as *distributions*.<sup>1</sup> In both cases the FT is a linear homeomorphism, but the *distributions* contains the largest class of functions we've encountered so far (and other operators as well). Dirac's function, the sinc function and any function in an  $L^p$  space are distributions.

We'll start by defining the *rapidly decreasing functions* and the topology on this set with which continuity will be defined. Then we'll state the results, and repeat the process for the *distributions*. Our spectroscopy is concerned with a domain of  $\mathbf{R}$ , but the results here are valid for  $\mathbf{R}^n$  and will be stated with that generality.

---

### Rapidly Decreasing Functions

---

The set of *rapidly decreasing functions*,  $\mathcal{L}_n$ , is a subset of  $C^\infty(\mathbf{R}^n)$ : the set of infinitely differentiable functions on  $\mathbf{R}^n$ . We'll use the following in defining them:

- Let the symbol  $\alpha = (\alpha_1, \dots, \alpha_n)$  represent multi-indices
- $|\alpha| = \sum \alpha_i$
- $D_\alpha = \frac{\partial^{\alpha_1}}{\partial x_1^{\alpha_1}} \cdots \frac{\partial^{\alpha_n}}{\partial x_n^{\alpha_n}}$

*Rapidly decreasing functions* are the subset of functions  $\phi \in C^\infty(\mathbf{R}^n)$  that satisfy

$$\sup_{|\alpha| \leq N} \sup_{x \in \mathbf{R}^n} (1 + |x|^2)^N |(D_\alpha \phi)(x)| < \infty \quad N = 0, 1, 2, \dots$$

---

<sup>1</sup>These are actually *tempered distributions*, but as this plays no role here we're using *distributions* for short.

Equivalently,  $\phi \in \mathcal{L}_n$  iff  $P \cdot D_\alpha \phi$  is a bounded function for all polynomials  $P$  and multi-indices  $\alpha$ . The expression on the left defines a semi-norm, and by a common application letting the sets

$$\sup_{|\alpha| \leq N} \sup_{x \in \mathbf{R}^n} (1 + |x|^2)^N |(D_\alpha \phi)(x)| < \frac{1}{N} \quad N = 0, 1, 2, \dots$$

be *open* defines a vector space topology that makes  $\mathcal{L}_n$  a Frechet space and brings us to our first result.<sup>1</sup>

---

## Fourier Transforms of Rapidly Decreasing Functions

---

### Theorem 3.6.1.

If  $\phi \in \mathcal{L}_n$ , then

$$\phi(x) = \int \hat{\phi} e^{ixt} dt \quad \forall x \in \mathbf{R}^n$$

The Fourier transformation is linear, continuous bijection  $\mathcal{L}_n \rightarrow \mathcal{L}_n$  and its inverse is also continuous.

This is a sufficient description, but the scope is too constricting as  $\mathcal{L}_n \in L^p$ ,  $\forall 1 \leq p < \infty$ <sup>2</sup> and we're requiring our functions to be infinitely differentiable. With  $R^2$  loss we would not expect our measured signal to be *rapidly decreasing* and therefore they're not in  $\mathcal{L}_n$ . The trick is then instead look at the continuous linear functionals on  $\mathcal{L}_n$ .

---

## Distributions

<sup>1</sup>A *Frechet* space is a locally convex space with a topology that is compatible with a complete, translationally invariant metric.

<sup>2</sup>This follows noting that  $|\phi(x)|^p \leq K^p/(1 + |x|^2)^p$ .



---

The topology defined on  $\mathcal{L}_n$  appends the qualifier *continuous* to certain linear functionals on this space, and denote the set of linear functionals satisfying the criteria  $\mathcal{L}'_n$ : the *distributions*. This is a very broad class of operators that includes the Dirac function, differential operators, measures, and any function in an  $L^p$  space. For example

**Definition 3.6.2.** *Let  $f$  be any function such that*

$$\int |f\phi| \, dm$$

*exists  $\forall \phi \in \mathcal{L}_n$  and is continuous on  $\mathcal{L}_n$ . Then we can associate the distribution*

$$\Lambda_f(\phi): \int f\phi \, dm$$

*with  $f$ .*

A specific case of this is for  $f \in L^p$ . Because  $\phi \in L^p \, \forall \, p$ , Hölder's inequality show that the integral on the right is finite. The operation is clearly linear and taking the difference of two such integrals, while noting the neighborhood definition in  $\mathcal{L}_n$ , shows that this is a continuous linear functional. Similar arguments also show that sinc is a distribution and that, without needing any further association, Dirac's function is linear and continuous- hence a distribution as it is.

By our previous result  $f \in \mathcal{L}_n \Rightarrow \hat{f} \in \mathcal{L}_n$ , therefore we can choose to extend the Fourier transform to  $\Lambda \in \mathcal{L}'_n$  by defining

**Definition 3.6.3.** *For  $\Lambda \in \mathcal{L}'_n$ , define its Fourier transform to be the distribution  $\hat{\Lambda}$  that satisfies*

$$\hat{\Lambda}(\phi) = \Lambda(\hat{\phi}) \quad \forall \phi \in \mathcal{L}_n$$

Using this, for  $f \in L^1, L^2$  and  $\forall \phi \in \mathcal{L}_n$ , we have

$$\hat{\Lambda}_f(\phi) = \Lambda_f(\hat{\phi}) = \int f \hat{\phi} = \int \hat{f} \phi = \Lambda_{\hat{f}}(\phi) \Rightarrow \hat{\Lambda}_f = \Lambda_{\hat{f}}$$

The equivalence of the integrals follows from Fubini's theorem for  $f \in L^1$  and by the Hilbert space isomorphism of the Plancherel transformation for  $f \in L^2$  (the integral is the inner-product). The equivalence of the outside terms, and our association of  $f$  with  $\Lambda_f$ , show that our *extension* is in agreement with both measure-theoretic results from the previous sections.

To get the complete statement of these results, we can take a common step and equip  $\mathcal{L}'_n$  with the *weak-\**-topology (pronounced *weak star*).<sup>1</sup>

---

## Fourier Transforms of Distributions

---

### Theorem 3.6.4.

*The Fourier transformation is linear, continuous bijection  $\mathcal{L}'_n \rightarrow \mathcal{L}'_n$  and its inverse is also continuous.*

In addition this transformation is in agreement with our previous measure theoretic results on  $L^1$  and the Plancherel transformation on  $L^2$ , and  $\mathcal{L}'_n$  includes:

- Dirac's function
- The sine function and the sinc function
- Any function in an  $L^p$  space
- Any polynomial
- Measures
- Differential operators

---

<sup>1</sup>This is the smallest topology on  $\mathcal{L}'_n$  such that evaluation on  $\phi$  is continuous  $\forall \phi \in \mathcal{L}_n$

and more. At this point we've reached our goal set out at the introduction and we can take some time to show the efficiency of our new FT in calculations and use this to derive a limit of the resolution of our spectrometer.

---

## §3.7 Using Distributions: Efficient Fourier Transform Calculations

---

Aside from it's theoretical value, the distributional results also give us the most efficient means with which to calculate Fourier transforms. The identified bijection allows us to choose which way we'd like to go, and the definition of a distribution's transform in 3.6.3 is a nice tool to work with. For example using this definition with  $\Lambda_{e^{-ita}}$ , the distribution associated with the  $e^{-ita}$  as in 3.6.2, gives

$$\hat{\Lambda}_{e^{-ita}}(\phi) = \Lambda_{e^{-ita}}(\hat{\phi}) = \int \hat{\phi} e^{-ita} dm = \phi(a) = \delta(x-a)\phi$$

As this is true  $\forall \phi \in \mathcal{L}_n$  we have that  $\hat{\Lambda}_{e^{-ita}} = \delta(x-a)$ : the Fourier transform of  $e^{-ita}$  is  $\delta(x-a)$  just like we'd expect. The bijection then gives us the opposite statement for free.

Another good example is the Fourier transform of the sinc function where the calculus derivations can be quite long. However noting that sinc and the indicator function  $1_{[-n,n]}$  are both in  $L^2$  and that our distribution results are in accord with the Plancherel transformation, we have (using  $\sim$  to denote the associations made between these functions and their distributions)

$$\hat{\Lambda}_{1_{[-n,n]}} \sim \hat{1}_{[-n,n]} = \int 1_{[-n,n]} e^{-ixt} dm = \frac{n}{\pi} \text{sinc}(nt) \sim \hat{\Lambda}_{\frac{n}{\pi} \text{sinc}(nt)}$$

Using the bijection and linearity, we then have that the transform of  $\text{sinc}(nt)$  is  $\frac{\pi}{n} \times 1_{[-n,n]}$ . The same integral could have been performed in any of the prior schemas, but this is the first instance in which we have grounds to reverse the statement and solve for sinc's transform (which can't be obtained legitimately via integration). As shown in §3.1, the FT of the sinc function can't be given

any significant meaning using the integral definitions of the transform alone. For our final task, we'll use these new results to estimate a limit on the resolution of our spectrometer.

---

## §3.8 Using Distributions: Estimating the Resolution of the Spectrometer

---



---

### Convolution

---

**Definition 3.8.1.** For  $\Lambda \in \mathcal{L}'_n$  and  $\phi \in \mathcal{L}_n$  we can define the convolution

$$(\Lambda * \phi)(t) = \Lambda(\tau_t \check{\phi})$$

where  $\check{\phi} = (\hat{\phi})^\wedge$  and  $\tau_t$  is the shift operator such that  $\tau_t \phi(x) = \phi(x - t)$ .

In the case that  $\Lambda$  is associated with a function as in 3.6.2 we get correspondence with the more classical definitions of convolution as then

$$\Lambda_f(\tau_t \check{\phi}) = \int f(y) \check{\phi}(y - t) \, dm = \int f(y) \phi(t - y) \, dm$$

where we've noted that  $\check{\phi}(x) = (\hat{\phi})^\wedge = \phi(-x)$  by 3.6.1. A more involved proof also shows that the familiar result

**Theorem 3.8.2.** For  $\Lambda \in \mathcal{L}'_n$  and  $\phi \in \mathcal{L}_n$

$$\hat{\Lambda} * \hat{\phi} = (\phi \Lambda)^\wedge$$

where  $\phi \Lambda \in \mathcal{L}'_n$  is the linear functional such that  $(\phi \Lambda)(\psi) = \Lambda(\phi \cdot \psi)$  for  $\psi \in \mathcal{L}_n$ .

The term on the left is a function, and the implication is that when it's associated with a linear functional as in 3.6.2 then it's equal to that on the right.

---

## Estimating the Resolution

---

Let's assume that our measured signal is  $\phi \in \mathcal{L}_n$  and that  $1_{[-L,L]}$  is the indicator function over the portion of the signal that we measured. Equivalently our measurement is  $1_{[-L,L]} \cdot \phi$ . The last calculation from the previous section showed  $\hat{1}_{[-L,L]} = \frac{L}{\pi} \text{sinc}(Lt)$ , whereby using 3.8.2 and 3.8.1

$$\left( \phi \cdot \Lambda_{1_{[-L,L]}} \right)^\wedge = \hat{\Lambda}_{1_{[-L,L]}} * \hat{\phi} = \Lambda_{\frac{L}{\pi} \text{sinc}(Lt)} * \hat{\phi} = \frac{L}{\pi} \int \hat{\phi}(y) \text{sinc}[L(t-y)] dm$$

Now the function associated with the linear functional on the left, namely  $1_{[-L,L]} \cdot \phi$ , is in  $L^p \forall p$ . Therefore (a) of 3.5.2 and the correspondence with the distributional transforms (3.6.4) show that, even by the calculus definition of the transform

$$(\phi \cdot 1_{[-L,L]})^\wedge = \frac{L}{\pi} \int \hat{\phi}(y) \text{sinc}[L(t-y)] dm$$

Now our sinc function peaks at 1 when  $y = t$ , has its first zeros when  $L|y - t| = \pi$  and doesn't rise above 0.2 afterwards. So when we're evaluating the convolution at a particular value of  $t$ , the values  $\hat{I}(y)$  for  $y$  outside a distance  $\pi/L$  aren't weighted much while those that are contribute some. Hence our convolution *distinguishes* values of  $t$  at least this distance apart and, noting that here  $L$  represents half the distance  $\delta$  over which we've made a measurement, we can estimate the resolution of our instrument to be at least  $\Delta t = 2\pi/\delta$ .<sup>1</sup>

We can confirm this with a citation:  $\Delta \bar{\nu} \geq 1/\delta$  (where  $\bar{\nu}$  denotes the linear wavenumber) [14]. Relating  $\bar{\nu}$  to the functions  $e^{-ixt}$  involved with the inversion formula (3.1.2), it follows that  $t\lambda = 2\pi \Rightarrow t = 2\pi\bar{\nu}$ . The cited limit is then equivalently  $\Delta t \geq 2\pi/\delta$  as was derived above.

---

<sup>1</sup>This derivation was modified from [13].

## 4 From Signal to Spectra

---

The previous section treated the Fourier transform as a purely mathematical object. Here the focus is on its implementation with measured interferograms. Excepting the methods used to identify axes of symmetry (§4.1) the techniques used here are strictly standard procedures although we will see that there are many options to choose from. Flow charts are used to help map the terrain.

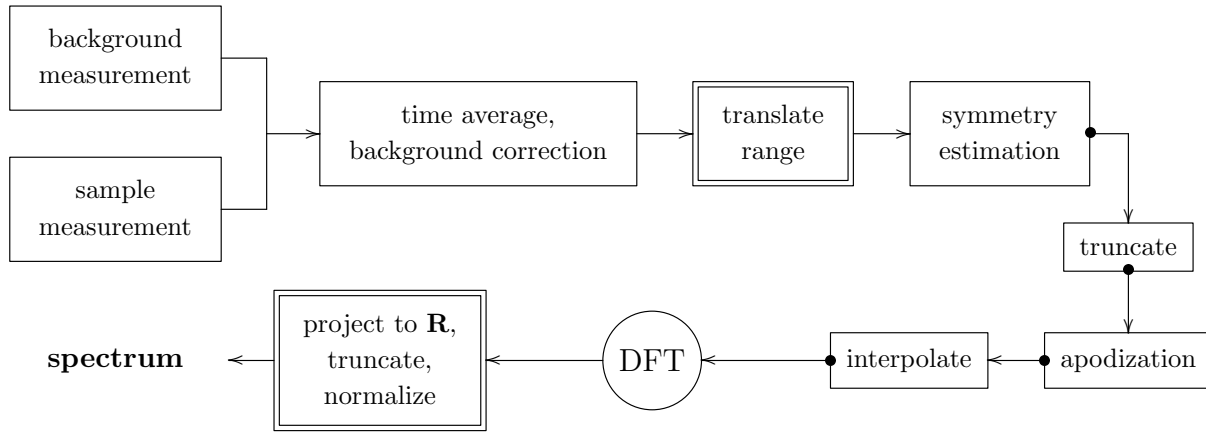
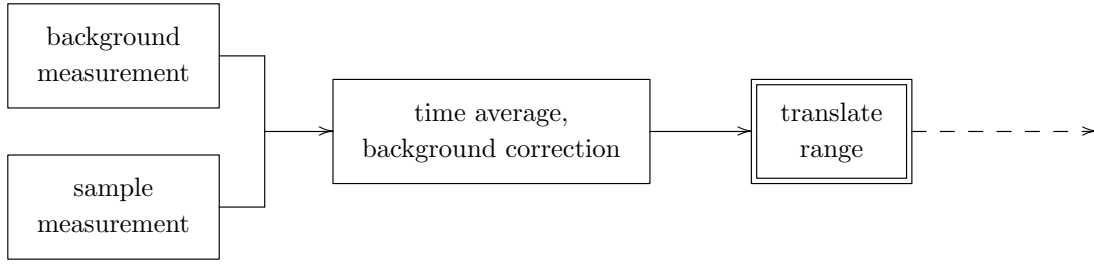


Fig. 4.0.1: The complete data processing schematic: from signal to spectrum. Bullets indicate where options are available in the processing techniques. The double box is also used to indicate an option between translating the range of the measured interferogram or truncating the result of its discrete Fourier transform (DFT).

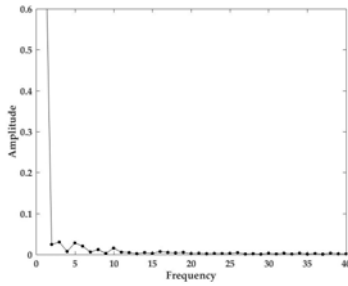
Each section below goes over a portion of this chart. In light of the options indicated in the figure, this experiment's data has been processed in 8 different ways. The appendix contains these results in full and provides complete descriptions of how these options were set. Overall there were drastic visual differences but, as virtually the same information intact, in a way the only changes are to aesthetics.

For convenience we'll use the notation  $(x, t, I)$  to represent a single data point where  $x$  denotes position,  $t$  time, and  $I$  the intensity read by the linear CCD array. A particular sample's measurement is then a set  $S$ :  $\{(x, t, I)\}$ . The first step in processing is to convert this, and the background

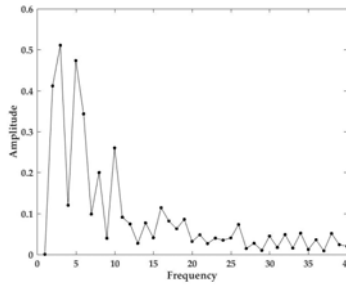
sample, into the time averaged sets  $\bar{S}: \{(x, \bar{I})\}$  and then make a background correction.



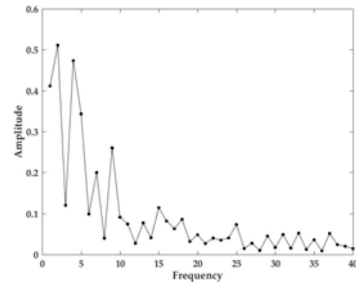
(a) The first steps are time averages and background corrections. Translating the range describes subtracting a constant from all intensity readings. This is described in detail later on. In the example below, the mean intensity has been subtracted.



(b) Only background correction



(c) Range translation



(d) Truncated constant term

Fig. 4.0.2: The same white light interferogram processed using three different settings. On the right, the constant term has been truncated post FT so that it doesn't dominate the signal as is shown on the left. Hence all three spectra are presenting virtually the same information but in aesthetically different ways.

As indicated in figure 4.0.1, there is an option between translating the range of the measured interferogram and truncating the result of the DFT. The difference is interesting when considered mathematically. Letting  $h = f - g$ , by the linearity of the FT the transformed signal is  $\hat{h} = \hat{f} - \hat{g}$ . Letting  $g$  be the indicator function on a finite interval, it's transform  $\hat{g}$  is a sinc function by §3.7. As translating is effectively subtracting a constant times the indicator function, we're equivalently subtracting a sinc function from the transformed signal  $\hat{f}$ . This is readily observed by comparing the truncated results in §B.3, which are highly oscillating, to the range translated results in §B.4.

These types of considerations give the processing techniques a circumstantial flavor, however we'll stick to the book while continuing to make analyses as above. The next step is to identify center-bursts in our interferograms.

---

## §4.1 Locating An Interferogram's Axis of Symmetry

---

Locating an interferogram's axis of symmetry is important because the FT is not translationally invariant. This can be seen using 3.1.1 with  $g(x) = f(x - \alpha) \in \mathcal{L}^1$ , which gives  $\hat{g}(t) = \hat{f}(t)e^{-\alpha t}$ .<sup>1</sup> Therefore in order for the FT to provide consistent results, position must be assigned to interferograms in meaningful way.<sup>2</sup> As interferograms are symmetrical about their centerbursts the most common thing to do is start there and consider an average of the two arms. Most of the interferograms measured here, however, had enough irregularities for this to not be straightforward and consequently five different estimators were used. The most likely culprits are the asymmetry inherent in the static design (see fig.1.0.2) and issues with collimation (see §2.2). Only 21 of the 87 measured interferograms were chosen for FT but we'll look at some of the others here as well to illustrate how these estimators behaved.

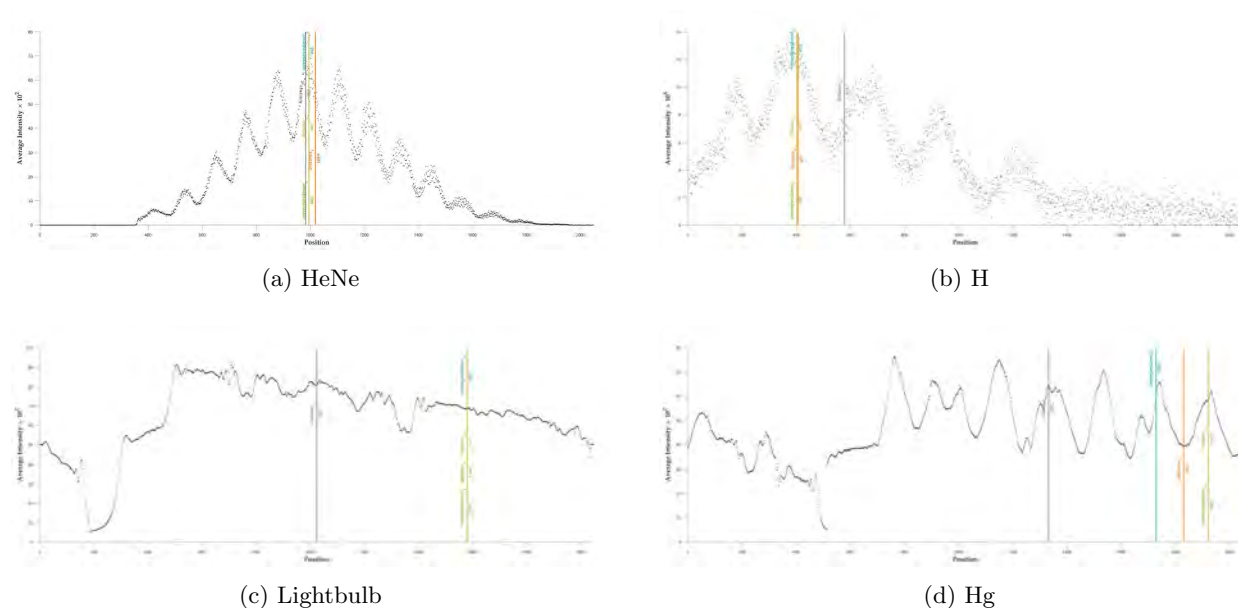


Fig. 4.1.1: Axes of symmetry produced by five different estimators. Most are in agreement with the more regular interferograms of HeNe and H at the top. The algorithm "distance loss 3" (DL<sub>3</sub>), shown in grey, seemed to better identify symmetries that were less obvious.

<sup>1</sup>Perform a change of variables and note the translational invariance of the Lebesgue measure.

<sup>2</sup>This was not built into the interferometer's construction and would have further complicated the issues with collimation (see §2.2).



Each of these estimators followed the same general scheme.



Fig. 4.1.2: The general scheme of the symmetry estimation. For brevity, in later flow charts the three steps in green will be subsumed under the single heading in black.

**Domain Eligibility:** First exterior points, prior to the interferogram crossing 3/4 of the distance from its minimum to maximum intensities, were excluded from candidacy. This was developed as a practical measure against pathologies.

**Pointwise Loss Evaluation:** For each eligible location, the symmetrical points about it were evaluated with a loss function (detailed below).

**Average Loss:** In the last step, the loss for the location was identified as the average of the pointwise losses evaluated above, and the location with the least loss was chosen as the axis of symmetry. If this was a tie, the location with the greatest intensity reading was chosen from the group.

Each estimator calculated pointwise loss using one of two loss functions  $\mathcal{L}_1, \mathcal{L}_2$ . To understand their operation, let  $x$  represent the location of an axis of symmetry that's being evaluated,  $x'_i$  be the mirror image of  $x_i$  about this axis, and let  $I(x'_i), I(x_i)$  represent the intensities measured at these respective points.

- $\mathcal{L}_1$ : correspondence loss.

For a given location  $x$ , this made pointwise calculations of  $|I(x'_i), I(x_i)|$  for all possible symmetric pairs  $x'_i, x_i$ . For example, if there were 300 CCDs to the left of  $x$  and 1747 to the right, there are only 300 symmetric pairs for which this calculation can be made.

- $\mathcal{L}_2$ : distance loss.

For a given location  $x$ , this made additional pointwise calculations of

$$\sqrt{w_I [I(y'_i) - I(x_i)]^2 + w_L [y'_i - x_i]^2}$$

for all  $y'_i$  within a certain range of  $x'_i$ . This range, and the weights  $w_I, w_L$ , were settings defined by the particular algorithm. In words,  $\mathcal{L}_2$ : allowed the mirror image  $x'_i$  to vary a little bit if this indeed minimized the weighted Euclidean metric above. This pointwise calculation was then performed regarding each such possible symmetric pair  $x'_i, x_i$  as in  $\mathcal{L}_1$  above. An arbitrary choice was made to consider  $x_i$  on the right side of the axis and let the  $y'_i$  vary on the left.

The removal of exterior points in the initial domain eligibility step then served to buffer against exterior locations where these average losses may be small only on account of there being few symmetric pairs  $x'_i, x_i$  to evaluate.

The five estimators used were:

- Correspondence Loss 1 (CL<sub>1</sub>)

This estimator is just as described in figure 4.1.2 using the pointwise loss function  $\mathcal{L}_1$ .

- Correspondence Loss 2 (CL<sub>2</sub>)

This is the same as CL<sub>1</sub> except locations  $< 300$  and greater than  $> 1748$ , along the 2048 linear CCD array, were automatically excluded from candidacy.

- Distance Loss 1 (DL<sub>1</sub>)

This estimator is just as described in figure 4.1.2 using the pointwise loss function  $\mathcal{L}_2$  under the conditions that  $y'_i$  could vary within a range of 50 from  $x'_i$ ,  $w_L = 1$  and

$$w_I = \left[ \frac{2048}{\max(\text{Intensity})} \right]^2$$

This last step was to weight the contributions of location and intensity evenly in the metric. However there is no scientific reason for doing this, particularly as units have not been considered.

- Distance Loss 2 (DL<sub>2</sub>)

This is the same as DL<sub>1</sub> except that the contributions of location and intensity have been weighted equally  $w_L = w_I = 1$ .

- Distance Loss 3 (DL<sub>3</sub>)

This estimator was unique. It's the same as DL<sub>2</sub> except that for all the possible symmetric pairs  $x'_i, x_i$ , DL<sub>3</sub> only evaluated the loss function  $\mathcal{L}_2$  on the pair furthest from the eligible axis' location. This single value was then taken to be the loss for the location, and DL<sub>3</sub> chose the location with the minimum loss. In words, this estimator only cared whether the point furthest from a given location appeared symmetric.

DL<sub>3</sub> originated as a programming error in DL<sub>2</sub> and was kept for it's unique success where there other estimators fail. Two examples of this were shown in figure 4.1.1 above and two more are in the figure below.

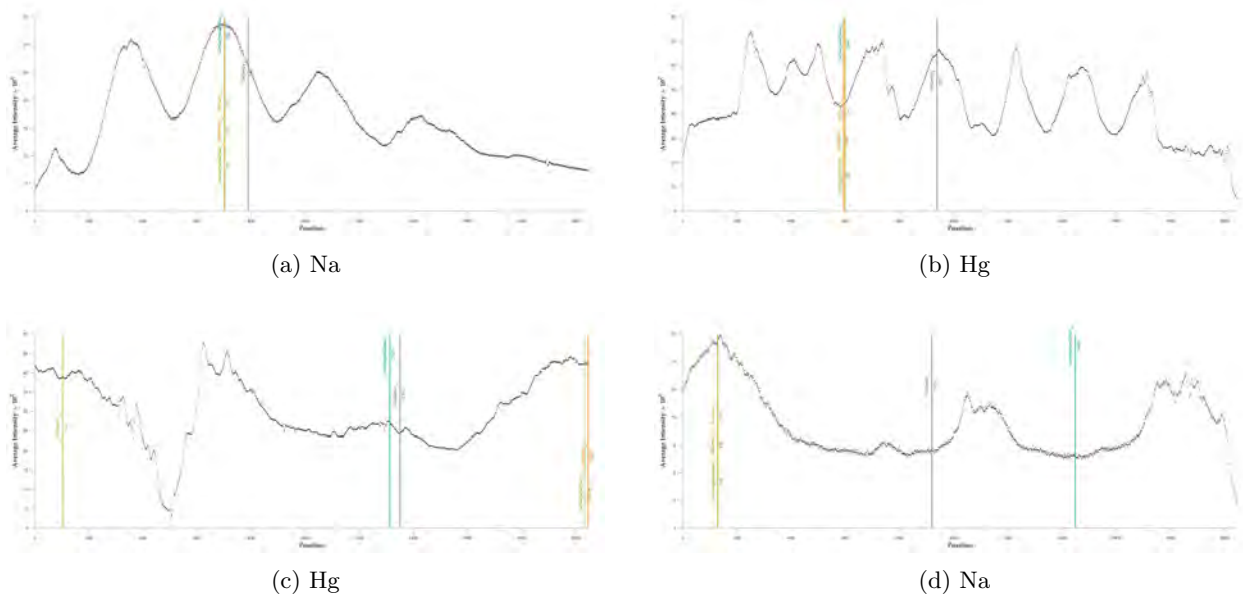


Fig. 4.1.3: The first is everyone winning and the last is everyone losing. In between we see  $DL_3$  (grey) again finding what generally is the most accurate axis of symmetry and its accompanied by  $CL_2$  (blue) on the bottom left.

An additional step was considered that performed each of the above calculations as the interferogram was rotated over a small range of angles. Estimators then minimized their loss over this larger set of possibilities. However this was a computational burden and presented its own set of pathologies and therefore was dropped.

After identifying a sample's axis of symmetry, a portion of the domain extending to the right, where there was a healthy signal, was chosen to comprise the surviving sample. There was no averaging of the two arms about the axis, as described in the introduction, as the signals were too asymmetric. This truncation is represented in the flow chart below and the necessary choices made with this, and selecting the which axis estimate to accept, have been indicated with bullets.

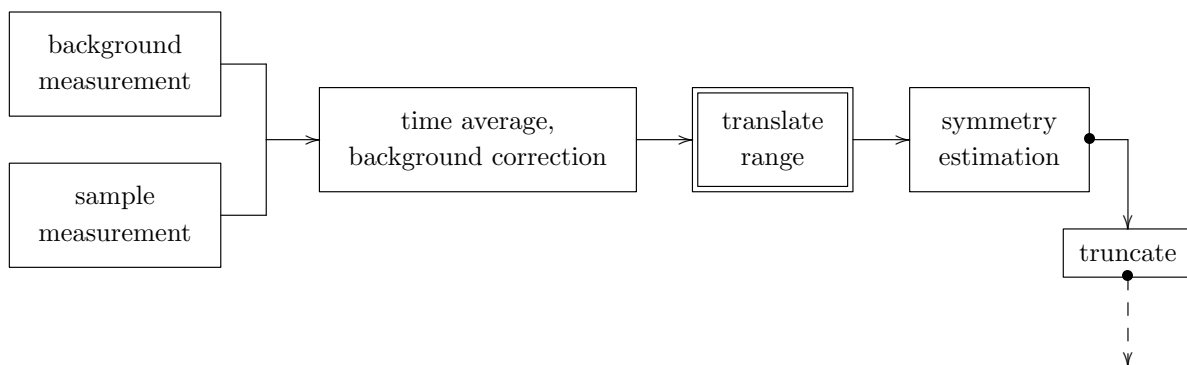


Fig. 4.1.4: At this point we've processed up to estimating symmetry and truncating the measured interferogram accordingly.

---

## §4.2 Apodization

---

Apodization is a technique used to smooth out the resulting FT. Beginning at the centerburst identified in the previous section, measurements are multiplied by some monotonically decreasing function  $\in [0, 1]$ .

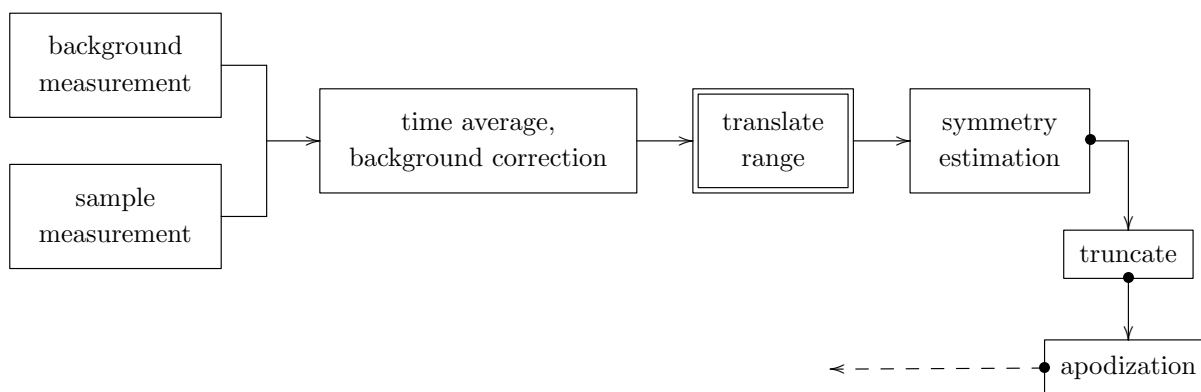


Fig. 4.2.1: There are options in choosing what apodization function to use. Linear and exponentially decaying functions are common choices.

A commonly cited reason for doing this follows from considering a continuous but finite measurement of a single frequency  $\cos(xt')$  [15],[16]. In this case we're equivalently measuring  $f(t) = 1_{[a,b]} \cos(xt') \in \mathcal{L}^1$  whose FT, by 3.5.1, has the real part

$$\text{Re}[\hat{f}(t)] = \int_a^b \cos(xt') \cos(xt) dx \propto \int_a^b \cos[x(t+t')] + \cos[x(t-t')] dt \propto \left|_a^b \frac{\sin[x(t+t')]}{(t+t')} + \frac{\sin[x(t-t')]}{(t-t')}\right|$$

The term on the right dominates as  $t \rightarrow t'$ , whereby  $\hat{f}(t)$  behaves locally like the sinc function.

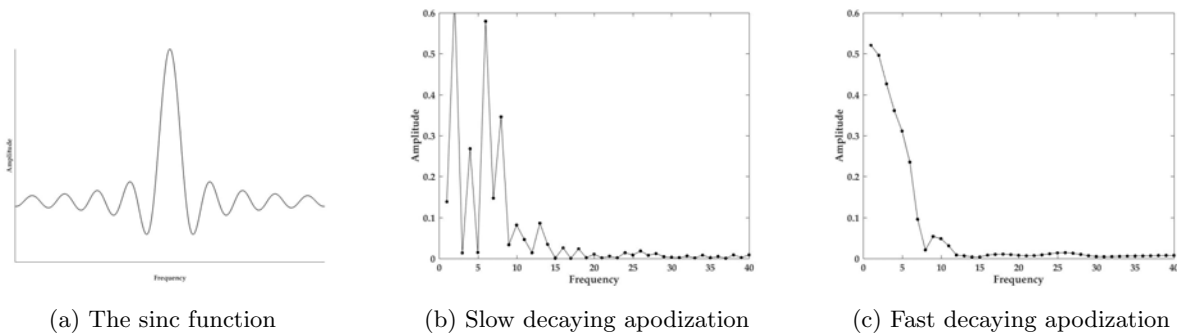


Fig. 4.2.2: The middle and right show the FT of the same Hg interferogram where apodization has been performed with a slowly decaying and rapidly decaying exponential, respectively. The more strongly apodized interferogram (probably too strongly) gives a smoother FT and we see the expected reduction in sinc behavior.

---

## §4.3 Implementing The Discrete Fourier Transform

---

There is one more step, interpolation, in processing before performing the discrete Fourier transform (DFT). However its easier to explain after covering the DFT so we'll do that first. The FT was covered in §3 and implicitly assumed that functions and their transforms were defined for every real number ( $x$  or  $t$ ). As our linear CCD array made only a finite amount of measurements and our computers can only perform a finite amount of calculations, implementing this warrants some extra attention.

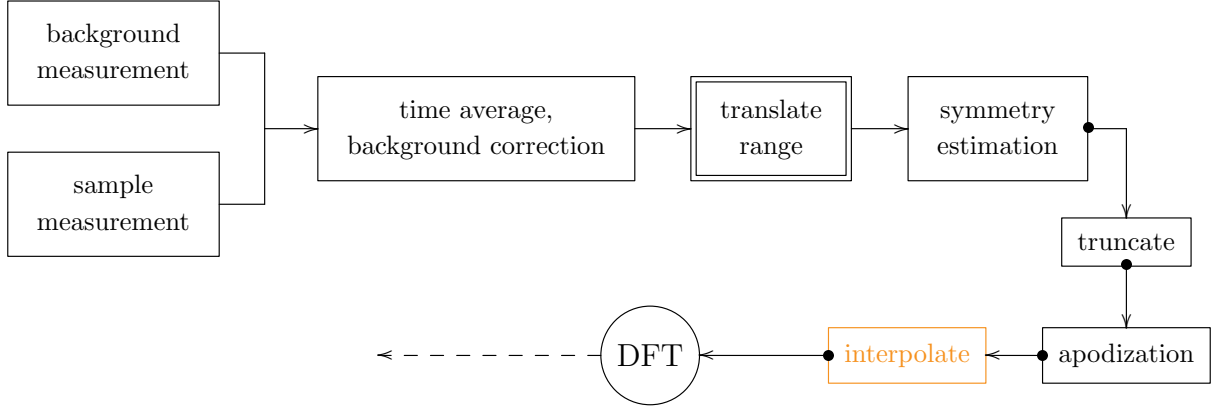


Fig. 4.3.1: Interpolation is another type of smoothing technique but its effects are more easily explained after covering the DFT.

We can consider our data processed up to this point as a finite collection of position and average intensity coordinates  $\bar{S}: \{(x_j, \bar{I}): 0 \leq j \leq n\}$ . Here  $x_0$  corresponds to the CCD at the interferogram's axis of symmetry and rest of the  $x_j$  number of the CCDs to its right. As shown in the introduction, the position on the CCD array is proportional to path displacement (see the paragraph under 1.0.3). Therefore, letting  $\delta_{\max}$  be the maximum path displacement occurring in  $\bar{S}$ , we can express  $x_j = j\delta_{\max}/n$  alternatively in terms of path displacement.

We also need to define the set of values  $T: \{t_0, t_1, \dots, t_m\}$  to evaluate the FT on. As derived and cited in §3.8, the resolution of an FT spectrometer is  $\Delta t_k \geq 2\pi/\delta_{\max}$ . This condition can be satisfied in many ways<sup>1</sup>, and we'll see how some of these can be inconsequential below, but an immediately obvious choice is letting  $t_k = k2\pi/\delta_{\max}$ .

This is also convenient as the exponential term in the FT integrand (3.5.1) becomes

$$e^{-ix_j t_k} = e^{-2\pi i(jk/n)} = (e^{-2\pi i/n})^{jk} = E^{jk} \quad E: e^{-2\pi i/n}$$

Because our average intensity  $\bar{I}$  is only defined on the  $x_j$ , it can be treated as a finite sum of step functions for integration purposes. The width of each step is irrelevant, because the FT is linear

<sup>1</sup>It would be interesting to explore any resulting differences.

and the result will be normalized, therefore we can make it 1. The pointwise FT of the measured interferogram  $\bar{S}$  is then explicitly

$$\hat{I}(t_k) = \sum_{j=0}^n I(x_j) E^{jk} \quad (4.3.2)$$

and, letting  $[I(x_j)]$  and  $[\hat{I}(t_k)]$  be column vectors, the entire FT can be expressed succinctly as

$$[\hat{I}(t_k)] = M[I(x_j)] \quad (4.3.3)$$

where  $M$  denotes the matrix with entry  $E^{jk}$  in row  $k$ , column  $j$ .<sup>1</sup> This is exactly how the DFT was implemented in Matlab, but if the results are kept for all the  $t_k$  it's immediately seen that there are two copies of the same information.

To see why this happens, fix an integer  $k'$  and let  $k_{\pm} = n/2 \pm k'$ . Then

$$E^{jk_{\pm}} = E^{j(n/2 \pm k')} = e^{-\pi i j} E^{\pm j k'}$$

As  $e^{-\pi i j} \in \mathbf{R}$ , it follows that  $E^{jk_{+}}$  is the complex conjugate of  $E^{jk_{-}}$ . By the linearity of the FT and 4.3.3 this means that  $|\hat{I}(t_{k_{+}})| = |\hat{I}(t_{k_{-}})|$  and their real parts are equal. Extending  $k$  past  $n/2$  only provides repeated data as a mirror image:  $t_{n/2}$  is known as the Nyquist frequency and calculating spectra beyond this limit is referred to as aliasing.

---

## §4.4 Interpolation

---

Interpolating is performed prior to the DFT but its discussion has been placed afterwards so that we can better describe what it does. In the previous section we noted that:

---

<sup>1</sup>Notice that  $M$  is symmetric.



- i) Practically, the DFT can only be calculated for a finite set of values  $\{t_k\}$ .
- ii) The resolution of an FT spectrometer requires that  $\Delta t_k \geq 2\pi/\delta_{\max}$
- iii) Using values of  $t_k$  greater than the Nyquist frequency doesn't provide any new information.

Interpolation is ignoring ii) and calculating the FT for values  $\tau_k$  with  $\Delta\tau_k < 2\pi/\delta_{\max}$ . This is what the name indicates but it's at odds with the most common descriptions of interpolation, zero-filling and mirror imaging, which are frequently justified on experimental grounds. Zero-filling amounts to concatenating series of zero intensities readings to what was actually measured by the instrument, and the justification is that this is likely true as the signal would die out over distance. Similarly mirror imaging concatenates a reflected image of the interferogram under the idea that the light source, or measured signal, are periodic. What we'll show here is that the specific ways in which zero-filling and mirror-imaging are done in practice amount to nothing more than was stated at the outset: calculating the FT for values  $\tau_k$  with  $\Delta t_k < 2\pi/\delta_{\max}$  (although we'll see that mirror-imaging also simultaneously maps these results to the reals). By making this statement precise we can understand the effects of interpolation in signal processing.

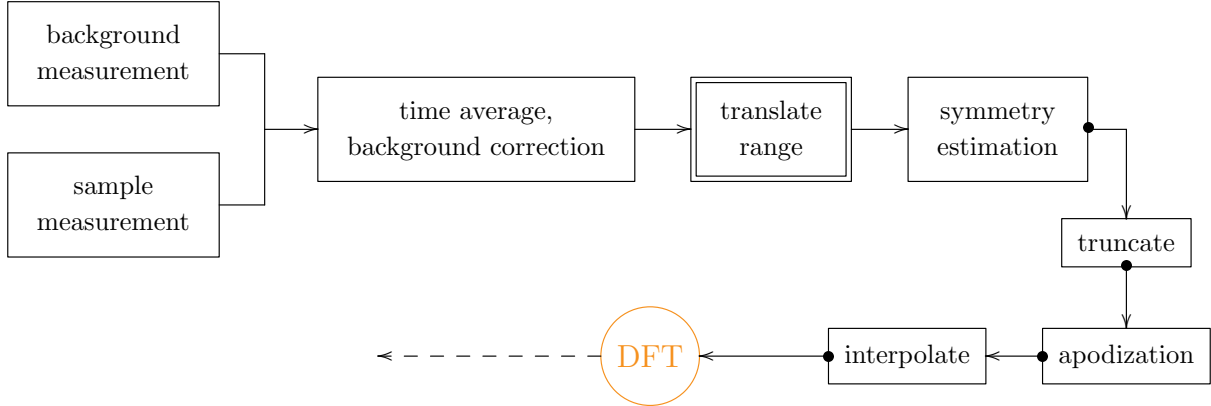


Fig. 4.4.1: Interpolation is discussed out of order because the language and results of the previous section are needed to explain what it does.

We'll begin with zero-filling, where the standard practice concatenate the actual measurements

$$\bar{S}: \{[x_0, \bar{I}(x_0)], [x_1, \bar{I}(x_1)], \dots, [x_n, \bar{I}(x_n)]\}$$

with a set

$$\bar{S}': \{[x'_1, 0], [x'_2, 0], \dots, [x'_{cn}, 0]\} \quad c \in \mathbf{N}^+$$

and adjust the actual maximum path difference  $\delta_{\max}$  to  $\delta'_{\max} = (c+1)\delta_{\max}$ . Let the concatenated set be

$$\bar{\mathcal{S}}: \{[\xi_0, \bar{I}(\xi_0)], [\xi_1, \bar{I}(\xi_1)], \dots, [\xi_{(c+1)n}, \bar{I}(\xi_{(c+1)n})]\}$$

where  $[\xi_i, \bar{I}(\xi_i)] = [x_i, \bar{I}(x_i)]$  for  $0 \leq i \leq n$  and the remaining points are zero-fills from  $\bar{S}'$ .

When performing the DFT on  $\bar{S}$  the previous section determined the value of  $n = |\bar{S}| - 1$ , so when done with  $\bar{\mathcal{S}}$  this value will be  $n' = |\bar{\mathcal{S}}| = (c+1)n$ . Similarly we have

$$x_j = j\delta_{\max}/n = j\delta'_{\max}/n' = \xi_j$$

as  $n'$  and  $j'$  have been scaled by the same constant. Therefore applying the FT (4.3.2) to  $\bar{\mathcal{S}}$  gives, for arbitrary  $t$ ,

$$\hat{\bar{I}}(t) = \sum_{j=0}^{n'} \bar{I}(\xi_j) e^{-i\xi_j t} = \sum_{j=0}^n \bar{I}(\xi_j) e^{-i\xi_j t} = \sum_{j=0}^n \bar{I}(x_j) e^{-ix_j t} = \hat{\bar{I}}(t) \quad (4.4.2)$$

where the expression on the right is the DFT of our original set of measurements  $\bar{S}$ .

Similarly, the values  $\{\tau_k\}$  at which the DFT of  $\bar{\mathcal{S}}$  will be evaluated satisfy

$$\tau_k = k2\pi/\delta'_{\max} = k2\pi/[(c+1)\delta] = t_k/(c+1)$$

Therefore by 4.4.2 the original spectra of  $\bar{S}$  is reproduced at intervals of  $(c + 1)$  and, equivalently, we could have simply used  $\bar{S}$  and additionally calculated the DFT for the interpolated values  $\tau_k$ .<sup>1</sup> This is illustrated in the figure below.

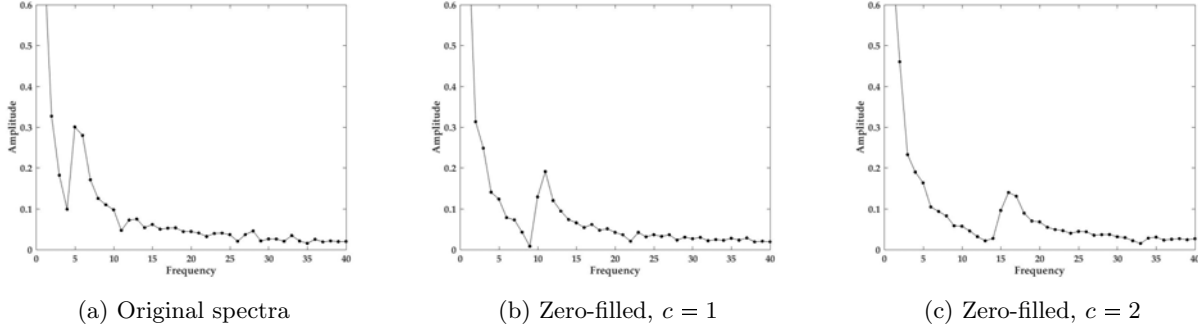


Fig. 4.4.3: Zero filling a HeNe interferogram. Notice the peaks at 5 and 6 in the original are located at 10 and 12 in the middle and 15 and 18 on the right (the intermittent points are new). The decrease in magnitudes is a consequence of normalizing after the DFT. In practice the frequency domain could be rescaled by  $1/(c + 1)$  for consistency but this was left out here to show the desired effect.

Mirror imaging accomplishes the same effect, under the assumption that the last intensity measured in the interferogram  $I(x_n) \approx 0$ , and maps the resulting DFT to the reals. The standard practice is here is to alternatively concatenate  $\bar{S}$  with the set

$$\bar{S}' : \{(x'_1, I(x_{n-1})), (x'_2, I(x_{n-2})), \dots, (x'_n, I(x_0))\}$$

and this result can again be denoted

$$\bar{S} : \{[\xi_0, \bar{I}(\xi_0)], [\xi_1, \bar{I}(\xi_1)], \dots, [\xi_{2n}, \bar{I}(\xi_{2n})]\}$$

where  $[\xi_i, \bar{I}(\xi_i)] = [x_i, \bar{I}(x_i)]$  for  $0 \leq i \leq n$  and the remaining points are  $\bar{S}'$ . The maximum path difference is also similarly adjusted to  $\delta_{\max}$  to  $\delta'_{\max} = 2\delta_{\max}$  and by §4.3 the DFT will be calculated for a set of values

$$\tau_k = k2\pi/\delta'_{\max} = k2\pi/(2\delta) = t_k/2$$

<sup>1</sup>If this was the goal, then there is a programming advantage to accomplishing it by zero filling as all one has to do is append zeros and run the existing DFT program.

Applying symmetry to the results at the end of the last section we can see that if  $j, j'$  are symmetrical indices about  $n/2$ , then  $E^{jk}$  and  $E^{j'k}$  are complex conjugates  $\forall k$ . Again referencing the DFT, transforming  $\bar{S}$  determined the value of  $n = |\bar{S}| - 1$  so with  $\bar{\mathcal{S}}$  this will be  $n' = |\bar{\mathcal{S}}| - 1 = 2n$ . Therefore  $E^{jk}$  and  $E^{j'k}$  are complex conjugates for indices  $j, j'$  that are symmetrical about  $n$ . But for such  $j, j'$  we also have  $I(\xi_j) = I(\xi_{j'})$  by the construction of  $\bar{\mathcal{S}}$ . Applying the FT (4.3.2) to  $\bar{\mathcal{S}}$  this then gives for arbitrary  $\tau_k$

$$\begin{aligned}\hat{\bar{I}}(\tau_k) &= \sum_{j=0}^{n'} \bar{I}(\xi_j) e^{-i\xi_j \tau_k} = 2\text{Re} \left\{ \sum_{j=0}^{n-1} \bar{I}(\xi_j) e^{-i\xi_j \tau_k} \right\} + \bar{I}(\xi_n) e^{-i\xi_n \tau_k} \\ &= 2\text{Re} \left\{ \sum_{j=0}^n \bar{I}(x_j) e^{-ix_j t_k/2} \right\} - (-1)^k \bar{I}(x_n) \\ &\approx 2\text{Re} \left\{ \hat{\bar{I}}(t_k/2) \right\}\end{aligned}$$

where the expression on the right is the DFT of our original set of measurements  $\bar{S}$  and we've noted that

$$\bar{I}(x_n) e^{-ix_n \tau_k} = \bar{I}(x_n) \left( e^{-2\pi i/n'} \right)^{(n'/2)k} = \bar{I}(x_n) e^{-2\pi i k} = (-1)^k \bar{I}(x_n)$$

The assumption that  $I(x_n) \approx 0$  was used in the final step.

As there's a normalization process following the DFT the factor of two is irrelevant and we can see that  $\hat{\bar{I}}(\tau_k)$  reproduces the original spectra at even  $k$  and provides the interpolated spectra at the odds.

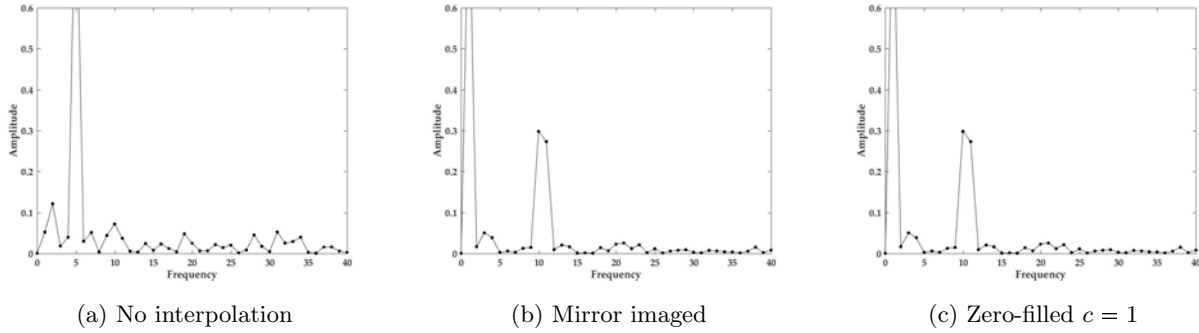


Fig. 4.4.4: The effects of mirror imaging a HeNe interferogram. The left is an FT of the interferogram that been mapped to the reals and normalized. The middle has only been mirror imaged and Fourier transformed: notice the peak originally at 5 is now at 10 on account of the interpolation. On the right the data was instead *zero-filled* ( $c = 1$ ) and mapped to the reals- accomplishing virtually the same result.

Interpolating too much tends to produce sinc behavior in the spectra and this effect is particularly strong when looking at the magnitude of the complex FT coefficients (§B.3, §B.4). In the past producing sets  $\bar{\mathcal{S}}$  whose order is a power of two has been relevant for the performance of Fast Fourier transform algorithms that implement the DFT, but no issues were encountered running the DFT as in 4.3.3 with Matlab.

---

## §4.5 Spectra and Units

---

Aside from a few minor details, our data processing is nearly complete. The remaining steps are projecting the result of the DFT to the reals, truncating off its constant term (in the case that the range hasn't been translated) so that it doesn't visually dominate the spectra, and finally normalizing.

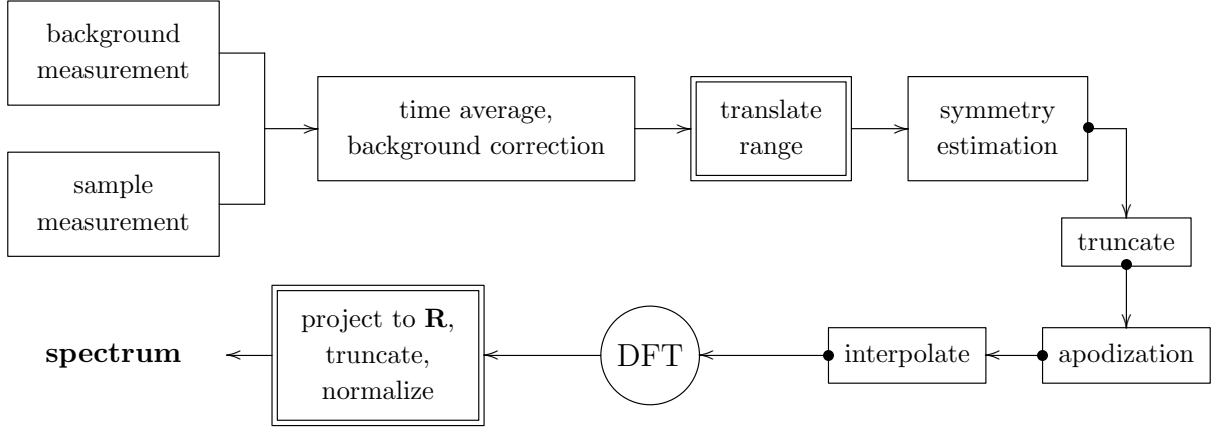


Fig. 4.5.1: The complete data processing schematic- from signal to spectrum. Bullets indicate where options are available in the processing techniques. The double box is also used to indicate an option between translating the range of the measured interferogram or truncating the result of the DFT. If the final truncation removes the constant term, range translation is not necessary (this is somewhat preferred, see §4.1).

In light of the options indicated in the figure, this experiment's data has been processed in 8 different ways. The full results are provided in the appendix along with the details of how these options were set, and sections B.7 and B.8 exemplify the most standard spectral processing. The latter was chosen to represent the spectral results of this experiment (§6) because it additionally incorporates an apodization function and represented a more complete procedure at the standard level.

For data mining purposes the last step in the process above has also been performed omitting projection to  $\mathbf{R}$ . The complex coefficients produced by the DFT, as well as their magnitudes, have both been graphed. In general, all the processing methods produced graphs with features useful in distinguishing samples by type.

As discussed in §1 there is an issue with estimating the maximum path difference  $\delta_{\max}$  with the design of the interferometer used in this work. Namely  $\delta_{\max}$  is introduced by screws on an adjustable mirror mount rather than something more precisely gauged like a micrometer. Looking at the FT inversion formula (3.5.1) we see that  $\hat{I}(t_k)$  weights a function  $e^{ixt_k}$  of wavelength<sup>1</sup>

<sup>1</sup>Note that the introduction showed that we're equivalently considering an average intensity  $\bar{I}_\lambda(\delta)$  that is a function of path displacement  $\delta$ , and that we've defined  $x_j = \frac{j\delta_{\max}}{n}$  in absolute units with respect to this dimension.

$$\lambda t_k = 2\pi \quad \Rightarrow \quad \lambda \left( \frac{k2\pi}{\delta_{\max}} \right) = 2\pi \quad \Rightarrow \quad \lambda = \frac{\delta_{\max}}{k} \quad (4.5.2)$$

and thus linear wavenumber  $\bar{\nu} = k/\delta_{\max}$ . Therefore we know the indices  $k$  are proportional to wavenumber but we don't know what the proportion is. In light of this we follow Aryamanya and Williams suggestion and determine our absolute units, hence resolution of the instrument, by comparison with known spectra [1]. However as the 21 Fourier transformed samples were measured using 8 different interferometers, this will only be done for a particular subset of four samples: one from each non-coherent light source that were measured on the same build. Consequently the graphs of the spectral results have been given arbitrary wavenumber units "Wavenumber (A.U.)."

As a final step, the results of our experiment require the unit analysis above be generalized for spectra processed with interpolation. In the notation of §4.4, the left side of 4.5.2 would then be considering  $\lambda\tau_k$  where

$$\begin{aligned} \tau_k &= t_k/(c+1) = \frac{k2\pi}{(c+1)\delta_{\max}} \\ \lambda &= \frac{(c+1)\delta_{\max}}{k} \quad (c+1) \in \mathbf{N}^+ \end{aligned} \quad (4.5.3)$$

$$\bar{\nu} = k/[(c+1)\delta_{\max}]$$

The second two equations simply applied the scaling in the first to our previous results. This makes sense intuitively as interpolation artificially increases the indices  $k$  by a factor of  $(c+1)$ : therefore we'd need to divide the frequencies of our final results at least on grounds for consistency. The case of  $c = 1$  is used in the experimental results.

## 5 Results and Discussion: Measured Spectra

---

This section presents selections of the FT spectra and makes qualitative and quantitative comparisons to known their known values. In total 21/87 of the measured samples were chosen for FT based on the quality of their measured signal and how well their axes of symmetry was found by the estimators (see §4.1). These samples were then Fourier transformed using 8 different variations of the general process outlined in §4. The full results and processing details are given in §B, and in particular variation detailed in §B.8 most emulated standard FT treatment and was chosen to furnish the samples here.

Four of these were then chosen to be representatives of their sample type, on the basis of having been measured by the same interferometer (the 21 initially selected were measured using 6 different builds) and being typical representatives, and these are compared qualitatively and quantitatively below.

As discussed in §4.5 and the introduction, absolute units must be assigned by comparison to known spectra on account of the maximum path difference being introduced by screws on an adjustable mirror mount rather than something more precisely gauged like a micrometer. Additionally the we know that the units of our output spectra are proportional to linear wavenumber (see §4.5).

Calibration will then be performed using two different methods. The first and most obvious is using HeNe's spectra but there are two problems with this.

- Given the construction it wasn't possible to achieve consistency between the paths of the HeNe and those of the non-coherent light sources. Non-coherent sources were necessarily sent through collimating optics prior to entering the interferometer. However this wasn't practical to do with the HeNe which, on account of its small high-intensity beam width, required that its recombined beam be magnified after leaving the interferometer in order to make the signal large enough, and low enough in intensity, to be read by the linear CCD array.



- Because of this shortcoming HeNe measurements were only made with the first of the nine interferometers built, and no other measurements were made with this interferometer.

Therefore the HeNe calibration will be used to provide a general estimate of how these instruments are performing. Using 4.5.3 with our  $c = 1$  interpolation gives

$$\delta_{\max} \approx \frac{k}{2\bar{\nu}} \quad (5.0.1)$$

where  $k$  is the unit-less integer output by our FT,  $\bar{\nu}$  is the linear wavenumber and  $\delta_{\max}$  is the maximum path difference introduced by the interferometer. As calibration by comparison provides the  $\bar{\nu}$ , we can then use the resulting  $\delta_{\max}$  to estimate the resolution of the instrument according to

$$\Delta\bar{\nu} = \frac{1}{\delta_{\max}} \quad (5.0.2)$$

as was derived and cited in §3.8.

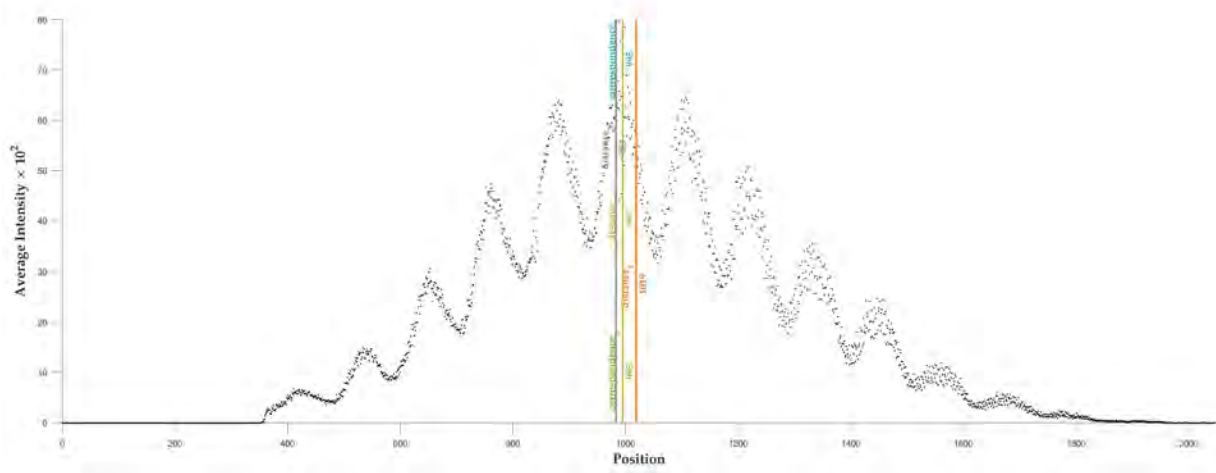
The more relevant calibration is performed with Na who's measured spectra showed the largest most recognizable peak in comparison with its known (see fig.5.2.1). The two calibrations will then be compared, and Na's will move on to perform the quantitative analysis amongst the four chosen samples above. Samples have been labeled by type and serial number as detailed in §2.6.

---

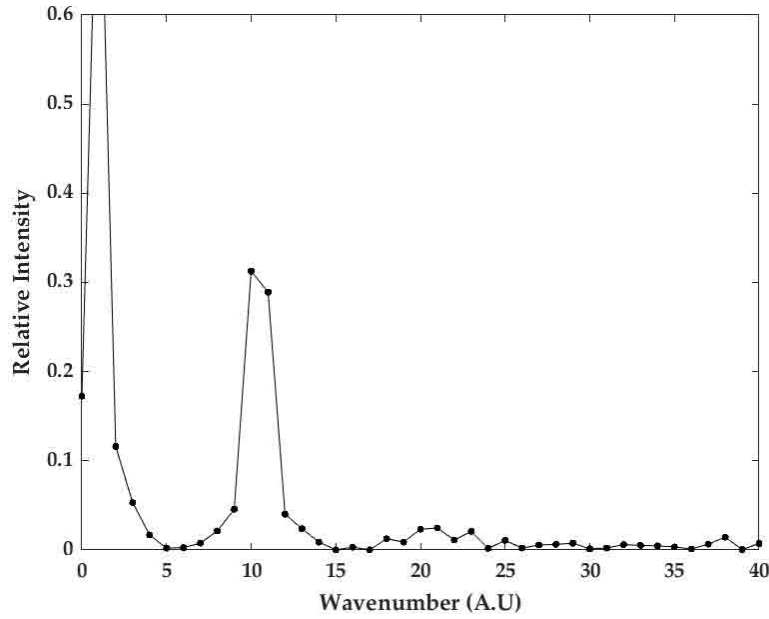
## §5.1 Calibrations with HeNe and Na Spectra

---

First we'll estimate the absolute units from a measurement of HeNe's spectra.



(a) The HeNe interferogram measured from sample 15.07.01.1.1316.32.HeNe



(b) The transformed HeNe spectra

Fig. 5.1.1: Measured HeNe interference and its Fourier transformed spectra. The center of the interferogram was chosen at 995 where three of the five estimators were in agreement. The initial spectral peaks around units 0 – 3 were observed with most spectra and therefore the unique peak at unit 10 was chosen to represent HeNe’s wavelength for calibrating.

The known HeNe peak lies at 632.8 nm ( $15803 \text{ cm}^{-1}$ ), therefore by 5.0.1 the maximum path difference is approximately

$$\delta_{\max} = 10/[2(15803 \text{ cm}^{-1})] \times \frac{10^4 \mu\text{m}}{\text{cm}} = 3.16 \mu\text{m}$$

In comparison, Zhan estimated the path difference in his static FT spectrometer to be  $\delta_{\max} = 30 \mu m$  [8]. This seems reasonable however the difference isn't favorable for our resolution which by 5.0.2 is estimated by

$$\Delta\bar{\nu} = \frac{1}{\delta_{\max}} = \frac{1}{3.16 \mu m} \times \frac{10^4 \mu m}{cm} \approx 3165 cm^{-1}$$

This an order of magnitude larger the typical range of  $200 - 350 cm^{-1}$  encountered in publications ([9, 5, 8]). This is can be expected as most citations were from research that had used different designs: most involving Wollaston prisms and Zhan's was a Sagnac interferometer.

Moving on, it's easy to see from figure 5.2.1 that the measured Na spectra does indeed give a very recognizable peak. This occurs and index  $k = 11$  in the measured spectra and at  $16978 cm^{-1}$  in the known, therefore repeating the methods above the maximum path difference is approximately

$$\delta_{\max} = 11/[2(16978 cm^{-1})] = 3.24 \mu m$$

Similarly the estimated resolution is

$$\Delta\bar{\nu} = \frac{1}{3.24 \mu m} \times \frac{10^4 \mu m}{cm} \approx 3087 cm^{-1}$$

and both of these values are in close agreement  $\pm 2.5\%$  with the HeNe calculations above. However amongst the 4/21 Fourier transformed Na samples (§B.8), 11 was the greatest location of the main peak while 5 was the lowest. Repeating the calculation above then puts  $\delta_{\max} = 1.47$  for the low peak and the two interferometers used to make Na measurements then differed by  $\pm 121\%$ .

---

## §5.2 Comparisons with Known Spectra

---

The four samples shown below were chosen on the basis of having been measured by the same interferometer (build 30.2) and being typical representations of the spectra measured for their sample type. First we give a qualitative comparison between the measured and known spectra of H, Hg, and Na

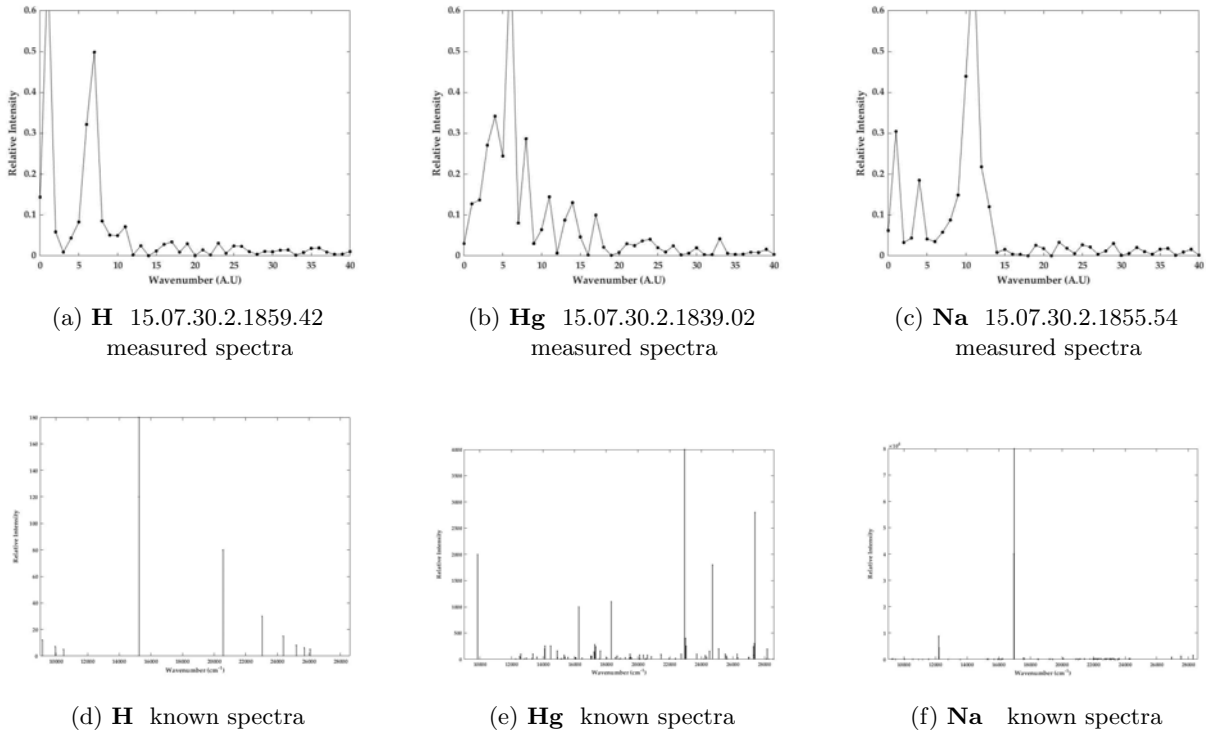
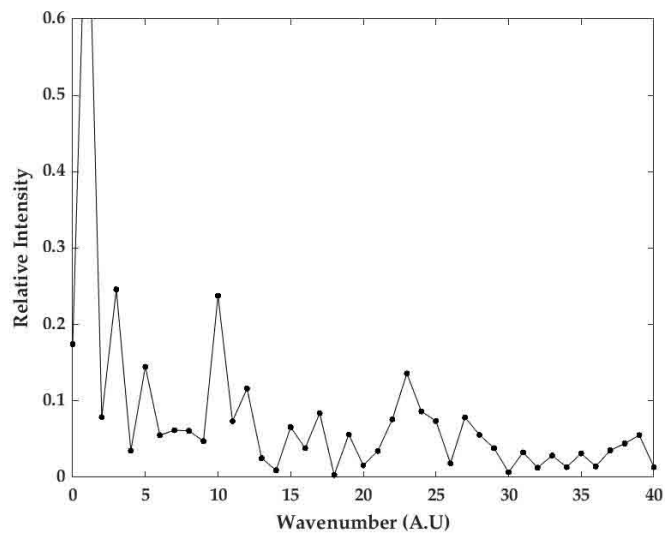


Fig. 5.2.1: Measured spectra in arbitrary units and known emission spectra in the 350 – 1100 nm specified range of the interferometer’s beamsplitter [17]. In general these, and the lightbulb’s spectra below, were characteristic and the spectra successfully distinguished the sources (see §B.8).



(a) **Lightbulb** 15.07.30.2.1828.58  
measured spectra

Fig. 5.2.2: The measured spectra of the lightbulb is qualitatively what's expected from a white-light source.

The following table uses the  $\delta = 3.24 \mu\text{m}$  calibration made in the previous section with Na's spectrum to estimate corresponding known peaks in figure 5.2.1.

Peaks Estimated from Na Calibration			
Element	Calibrated Peak ( $\text{cm}^{-1}$ )	Actual Peak ( $\text{cm}^{-1}$ )	$ \text{Error} /\Delta\bar{\nu}$
H	10804	15237	1.44
Hg	16978	16261	0.23
Hg	21608	22945	0.43
Hg	26239	24712	0.49

Table 5.2.3: With the given calibration, the resolution of the instrument is estimated as  $\Delta\bar{\nu} = 3087 \text{ cm}^{-1}$ . The third column gives the error in terms of this factor.

In all cases but H, the errors are well within the resolution limits but it's overwhelmingly clear that ultimately the resolution of the instrument needs to be improved.

## 6 Results and Discussion: Data Mining

---

The instrument in this experiment collected a new kind of interferogram data:  $\{\bar{I}(x, t)\}$  where  $\bar{I}$  is average intensity and  $x, t$  are position and time, respectively. In total 87 interferograms were sampled using 8 different interferometers. The entirety of each interferogram was measured simultaneously 100 times at 5 *ms* intervals. When performing the FT this new information was discarded in time averaging, and the purpose of this section is to go back and see if there was anything useful in the full data set. Specifically we'll be looking into whether it's viable to use the new data set to identify the sample type being measured, and this will play out in three stages.

- i) First this data will be graphed in several ways to help qualitatively expose underlying trends.
- ii) Second, a probabilistic model will be created so that the performance of these trends can be described with statistical significance.
- iii) Last is quantifying the trends and statistically analyzing the results.

As each interferogram's measurement consists of 204,800 data points, the word viable is appended to indicate that solutions that are simply over-trained on the collective data will be omitted. Our first step is to take a qualitative look at the data. Samples have been labeled by type and serial number as detailed in §2.6.

---

### §6.1 Qualitative Trends

---

This section presents the results of the graphical methods in qualitatively identifying trends in the new interferogram data. For each method, graphs for the complete collection of 87 measured

interferograms is presented, and organized by sample type, in §A. One sample from each non-coherent source has been chosen to be a constant representative throughout the presentation below. The first plots are histograms, created using using the new  $\{\bar{I}(x,t)\}$  data, which give an idea of what was actually recorded by the linear CCD array. These were plotted using both spatial and time domains, the former being processed according to

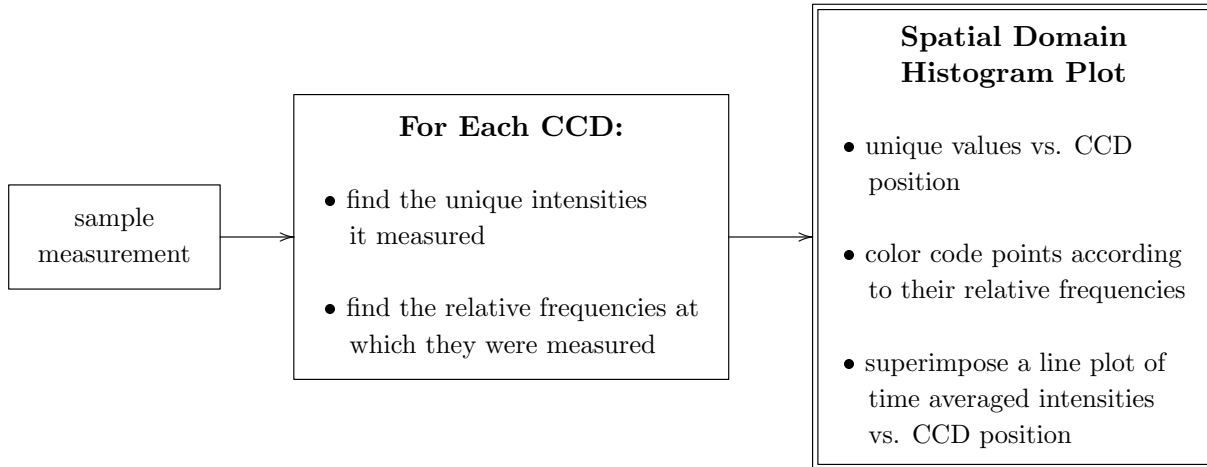


Fig. 6.1.1: Processing the spatial domain histograms from the measured interferograms.

The four examples shown below typify their respective non-coherent sources.

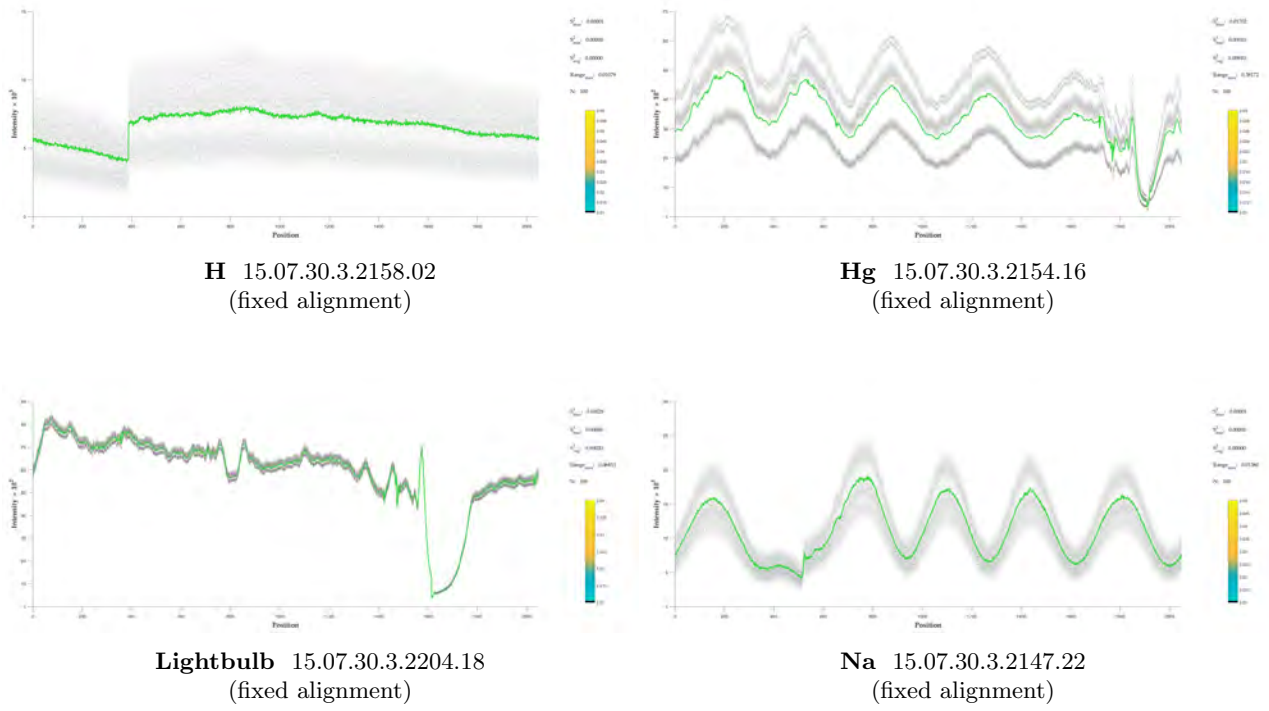


Fig. 6.1.2: Characteristic spatial domain histograms of the four non-coherent sources.

Two characteristics observed in these graphs have been successfully quantified below:

- The band gaps, which are characteristically wide with Hg, distinguish sample types with 95.4% accuracy.
- The mean fixed-position variance distinguishes sample types with 91.9% accuracy.

Collectively there was also a strong trend for the time-averaged intensities to be located in, or adjacent to, band gaps. With the lightbulb, this can be seen by enlarging the figure above.



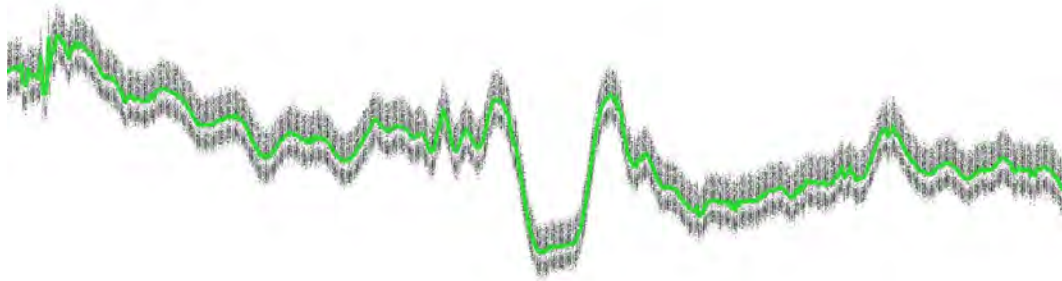


Fig. 6.1.3: A closer look at the plot of sample Lightbulb 15.07.30.3.2204.18 in figure 6.1.2. The average plot is systematically located just above a band gap.

Moving on, the time domain histograms were processed symmetrically by interchanging the roles of  $x$  and  $t$ .

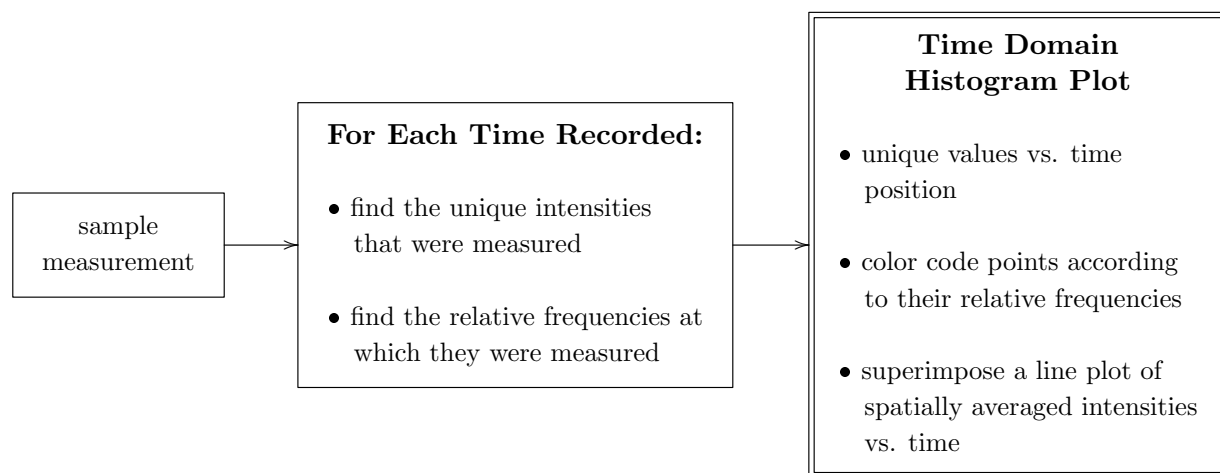
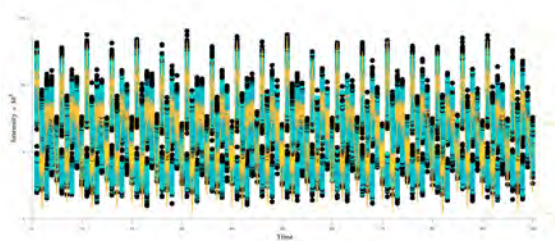
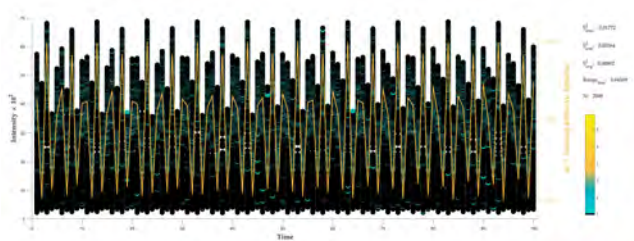


Fig. 6.1.4: Processing the time domain histograms from the measured interferograms.

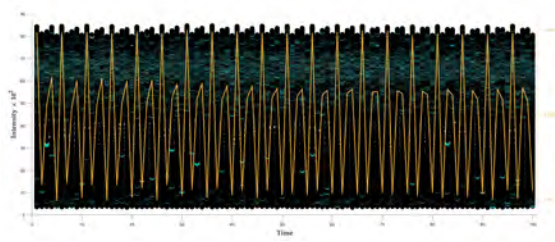
The sample types had characteristic colors indicating different trends in the relative frequencies at which intensities were measured. There are also typical behaviors in how each time's maximum and minimum intensity changed while moving sequentially forward time.



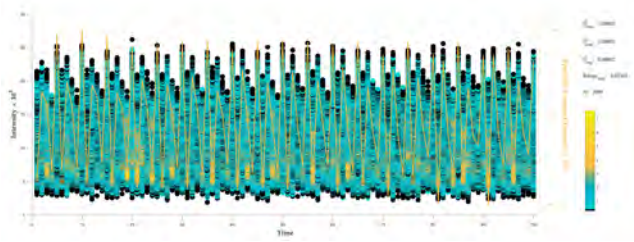
**H** 15.07.30.3.2158.02  
(fixed alignment)



**Hg** 15.07.30.3.2154.16  
(fixed alignment)



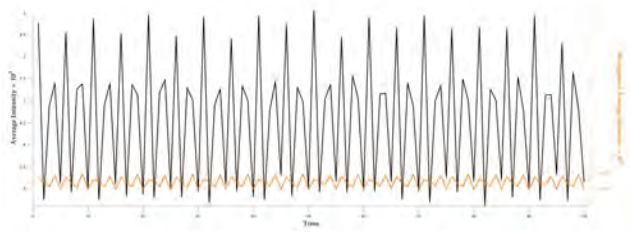
**Lightbulb** 15.07.30.3.2204.18  
(fixed alignment)



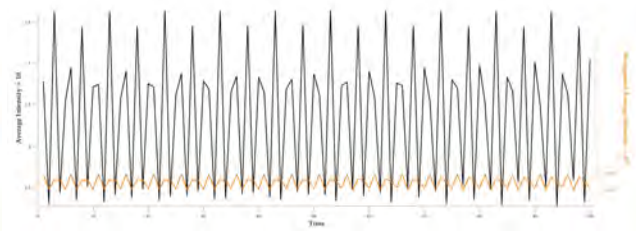
**Na** 15.07.30.3.2147.22  
(fixed alignment)

Fig. 6.1.5: Characteristic time domain histograms of the four non-coherent sources.

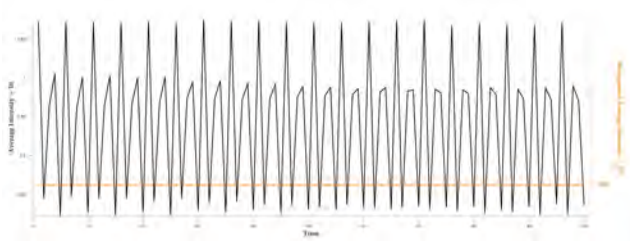
By removing the histogram points, it can be seen that the behavior of the extrema is mirrored in the spatially averaged intensities.



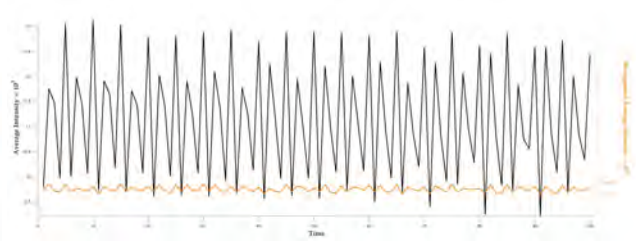
**H** 15.07.30.3.2158.02  
(fixed alignment)



**Hg** 15.07.30.3.2154.16  
(fixed alignment)



**Lightbulb** 15.07.30.3.2204.18  
(fixed alignment)

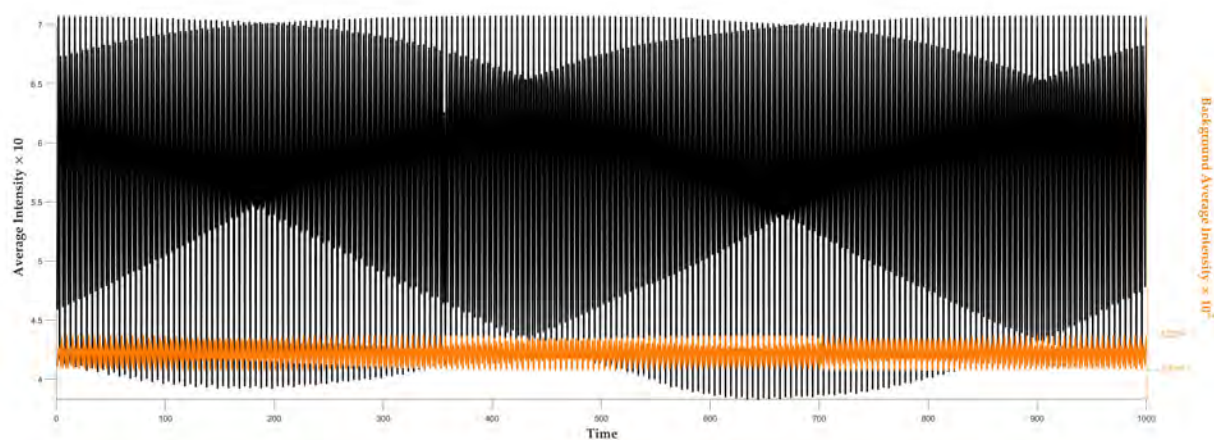


**Na** 15.07.30.3.2147.22  
(fixed alignment)

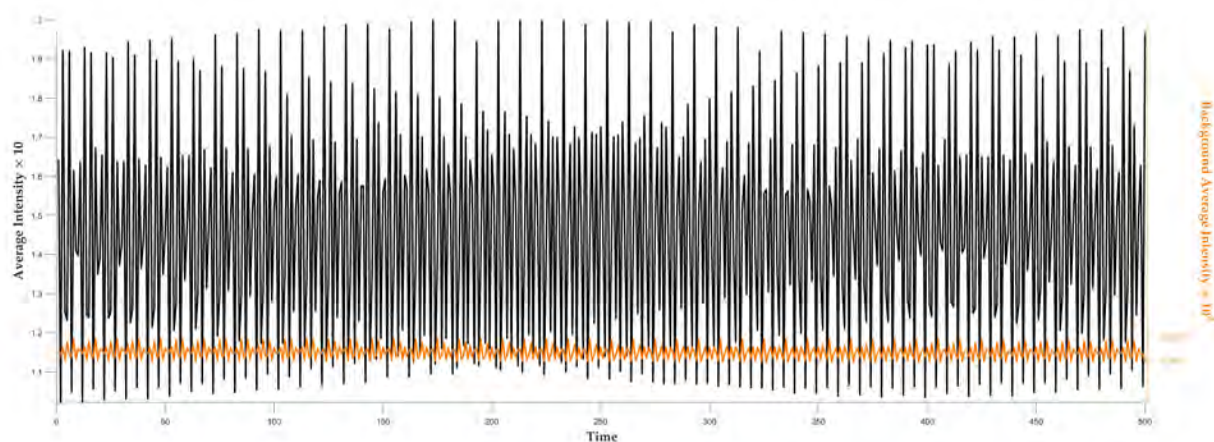
Fig. 6.1.6: Spatially averaged intensities of the four non-coherent sources. The background measurements are plotted separately in orange with the same scaling.

In the measurements made with one interferometer, build 22.1, the measurement period was increased by a factor of 10.<sup>1</sup> In this the distinction between the measured samples became much more prominent.

<sup>1</sup>This method was discontinued as the resulting 2,048,000 data points made for sluggish .csv files.



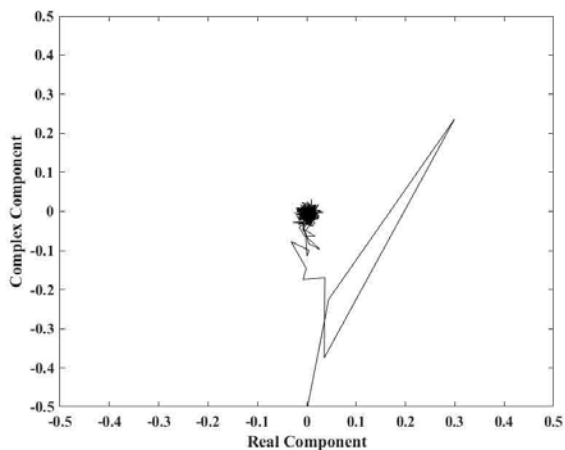
**Hg** 15.07.22.1.0952.02  
(near zero path length)



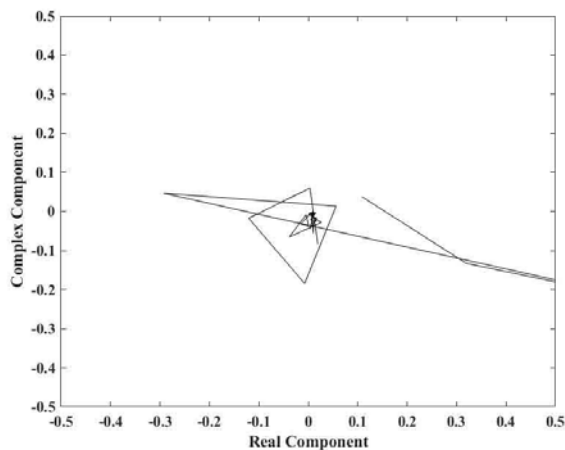
**Na** 15.07.22.1.0924.30  
(near zero path length)

Fig. 6.1.7: Spatially averaged intensities from interferometer build 22.1, where the measurement period was increased by a factor of ten (only Hg and Na were measured). The background measurement is plotted in orange with the same scaling.

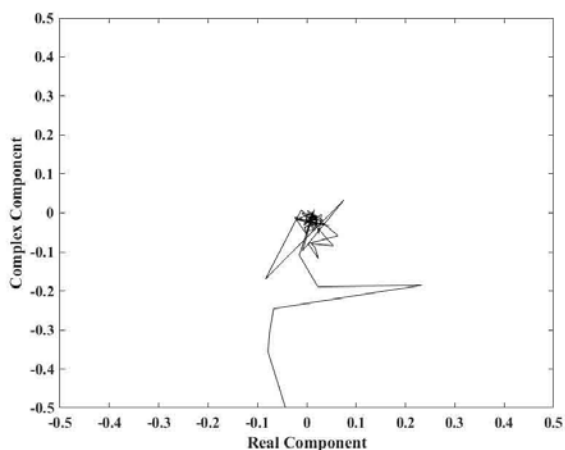
Finally, the last trends examined were the actual complex coefficients resulting from the FT, and these were plotted in the complex plain.



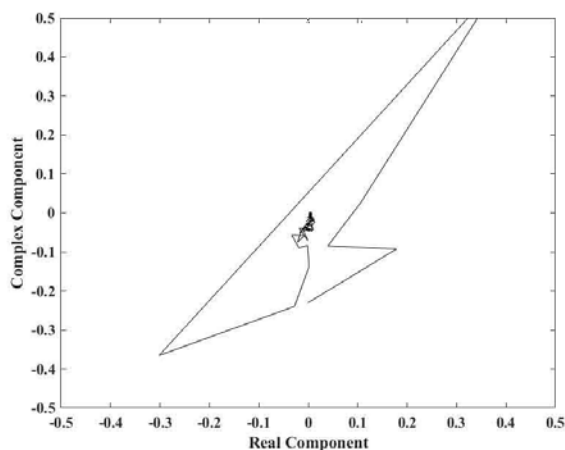
**H** 15.07.30.2.1859.42  
(fixed alignment)



**Hg** 15.07.30.2.1839.02  
(fixed alignment)



**Lightbulb** 15.07.30.2.1828.58  
(fixed alignment)



**Na** 15.07.30.2.1855.54  
(fixed alignment)

Fig. 6.1.8: Plots of the Fourier transformed coefficients in the complex plane. Because the FT processing projects these values to the magnitudes of their real parts, these graphs, in full resolution, contain more information than the FT spectra.

This concludes the presentation of the qualitative results. Now we'll briefly look at the probabilistic model used to determine the statistical significance and then see how the quantified versions of a few of these trends perform.

---

## §6.2 Probabilistic Modeling and Statistical Significance

---

The purpose of this section is to develop a probabilistic model that will allow the performance of quantified data trends to be described with statistical significance. To do this, let's take a look at how a random assignment  $\mathcal{A}_r$  would identify these samples.

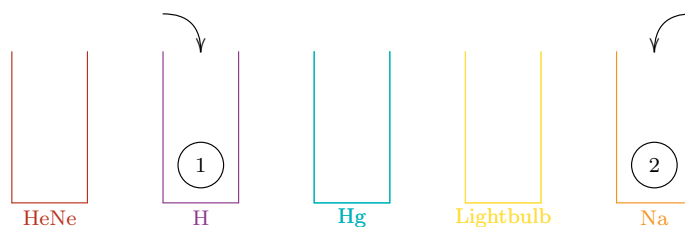


Fig. 6.2.1: A simplified description of how samples would be identified by random assignment  $\mathcal{A}_r$ .  $\mathcal{A}_r$  places  $n$  individual samples randomly into one of the  $m$  buckets representing identification. Each placement is independent from the rest and has a probability of  $\frac{1}{m}$  of being correct: therefore the number of correct decisions made by  $\mathcal{A}_r$  has a binomial( $n, \frac{1}{m}$ ) distribution.

When considering the assignments  $\mathcal{A}$  made by a quantified trend, we can then use the null hypothesis

$$\mathcal{H}_0: \mathcal{A} = \mathcal{A}_r$$

In words, that our trend  $\mathcal{A}$  has no basis and is simply identifying samples at random. This hypothesis will be rejected if and only if  $\mathcal{A}$  identified so many samples correctly that  $\mathcal{A}_r$  would have less than a 5% chance of matching that performance. This is represented by the top 5% tail of the binomial distribution.

The only problem with this is that our experiment consists of  $n = 87$  samples of  $m = 5$  different types and these conditions make it too easy for a trend to be significantly better than  $\mathcal{A}_r$ . For example, correctly identifying only 25/87 samples would reject the null hypothesis in our size 0.05 test with a  $p$ -value of 0.0325. This is a consequence of  $\mathcal{A}_r$  only making correct identifications with a probability of 0.2. Demonstrating significantly better performance than  $\mathcal{A}_r$  suggests that there's something meaningful in a trend but it's not a very useful result.

Therefore to make things more stringent we will instead use null hypotheses based on assignments  $\mathcal{A}_p$  that have a probability  $p \in \{0.7, 0.75, 0.8, 0.85, 0.9\}$  of making correct identifications.

$$\mathcal{H}_{0,p}: \mathcal{A} = \mathcal{A}_p$$

These will be treated separately and in each case, as in the above, we will only reject  $\mathcal{H}_0$  if  $\mathcal{A}$  has identified so many samples correctly that  $\mathcal{A}_p$  would have less than a 5% chance of matching that performance. Each test was performed and output, along with its  $p$ -values, simultaneously by Matlab. The  $p$ -value of the test for the highest-probability  $\mathcal{A}_p$  for which  $\mathcal{H}_{0,p}$  was rejected is reported below as a statistical description of the performance of  $\mathcal{A}$ .

---

## §6.3 Quantitative Results

---

This section presents quantified versions of a few of the trends observed in the qualitative section above and statistically analyzes their performance. To ease the notation, we'll consider the our data set  $\{\bar{I}(x, t)\}$  as an  $M \times N$  array with entries  $\bar{I}_{m,n}$ , where  $1 \leq m \leq M$  corresponds to the values of  $x$  (the CCD positions) and  $1 \leq n \leq N$  corresponds to the times of measurement (which were made at 5 *ms* intervals). In all cases quantification involves mapping samples to scalar value.

The first trend we'll treat is the time variations of the intensity measurements observed in figure 6.1.2. This was quantified by the scalar  $\bar{V}$  which was processed by

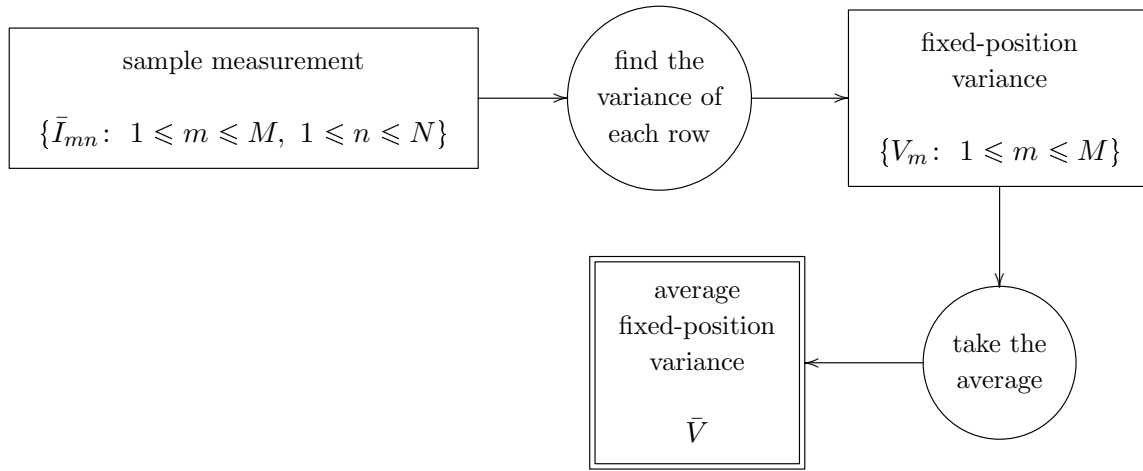


Fig. 6.3.1: Processing the scalar  $\bar{V}$  to quantify the observed time variations in intensity measurements. The computations involved in data processing are represented in circles.

The values of  $\bar{V}$  were then categorized by sample type and analyzed with descriptive statistics

### $\bar{V}$ by Sample Type (A.U.)

	HeNe	H	Hg	Lightbulb	Na
<b>mean</b>	$3.83 \times 10^{-3}$	$3.30 \times 10^{-6}$	$1.28 \times 10^{-2}$	$1.96 \times 10^{-4}$	$1.36 \times 10^{-4}$
<b>median</b>	$4.06 \times 10^{-3}$	$3.27 \times 10^{-6}$	$1.50 \times 10^{-2}$	$2.00 \times 10^{-4}$	$1.25 \times 10^{-5}$
<b>standard deviation</b>	$1.28 \times 10^{-3}$	$1.29 \times 10^{-6}$	$4.05 \times 10^{-3}$	$4.06 \times 10^{-5}$	$3.41 \times 10^{-4}$
<b>minimum</b>	$2.15 \times 10^{-3}$	$2.17 \times 10^{-6}$	$3.96 \times 10^{-3}$	$1.34 \times 10^{-4}$	$2.66 \times 10^{-6}$
<b>maximum</b>	$5.03 \times 10^{-3}$	$4.48 \times 10^{-6}$	$1.93 \times 10^{-2}$	$2.85 \times 10^{-4}$	$1.14 \times 10^{-3}$

Table 6.3.2: Descriptive statistics of  $\bar{V}$  by sample type.

which were then used to optimize threshold ranges for identifying the samples.



## Samples Identified by Values of $\bar{V}$

Sample Type	Thresholds		# of Samples Identified	
	Minimum	Maximum	Correctly	Incorrectly
HeNe	$2.15 \times 10^{-3}$	$3.55 \times 10^{-3}$	2	2
H	$2.17 \times 10^{-6}$	$2.19 \times 10^{-6}$	2	2
Hg	$3.96 \times 10^{-3}$	$1.93 \times 10^{-2}$	27	0
Lightbulb	$1.34 \times 10^{-4}$	$2.49 \times 10^{-4}$	28	0
Na	$2.66 \times 10^{-6}$	$2.79 \times 10^{-5}$	21	3
<b>Totals</b>			80	7
			91.9% correct	
			$p = 0.04$ vs. $\mathcal{A}_{0.85}$	

Table 6.3.3: The  $p$ -value shows that sample identification with a strategy  $\mathcal{A}_{0.85}$ , that has an 85% probability of correctly identifying individual samples, would have less than a 4% chance of correctly identifying this many samples.

The second trend we'll look at is the band gaps (see figure 6.1.2). A first attempt quantified this by the scalar  $D$ , which captures the time discontinuities in the measured intensities. This was processed from the raw data by the process

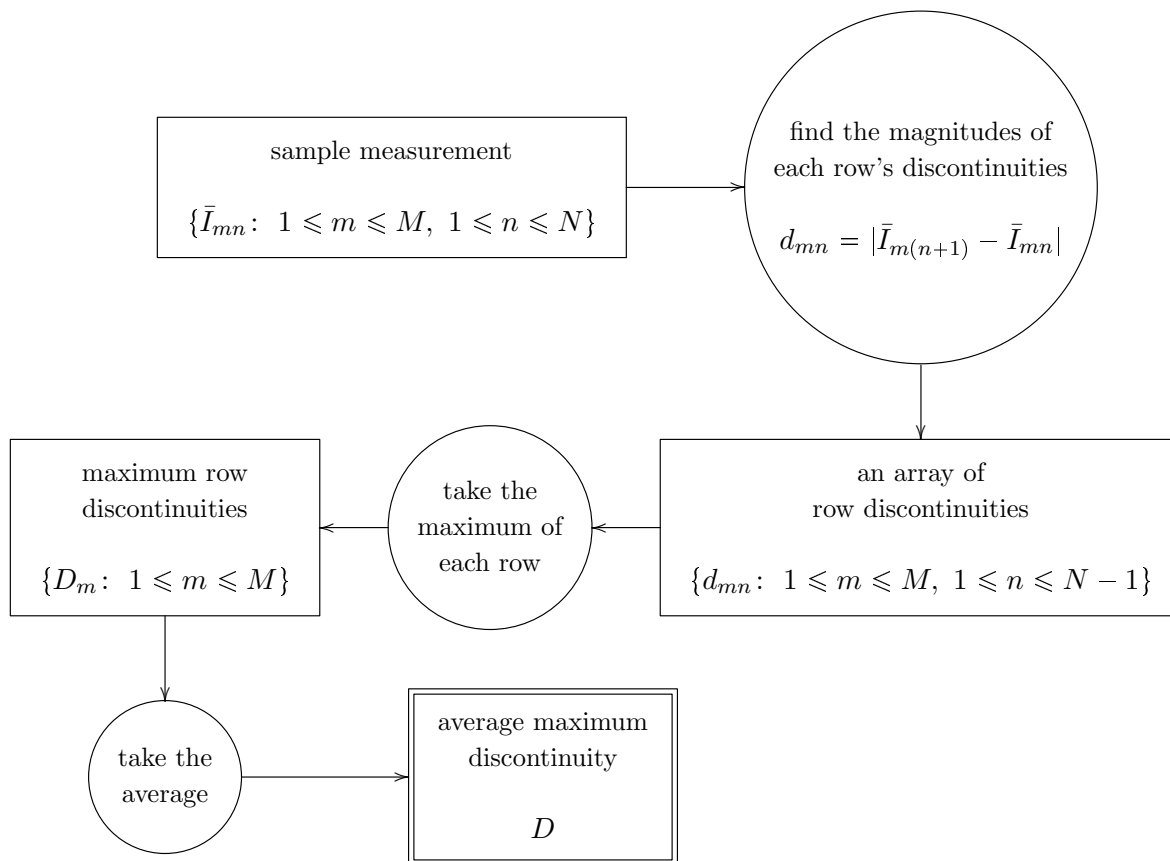


Fig. 6.3.4: Processing the scalar  $D$  to quantify the time discontinuities in intensity measurements. Background intensities were negligible but in this case a background correction would also be nullified in the first step and wouldn't effect the result.

As before, descriptive statistics of  $D$  were analyzed within sample types

### $D$ by Sample Type (A.U.)

	HeNe	H	Hg	Lightbulb	Na
<b>mean</b>	0.205	$6.11 \times 10^{-3}$	0.301	$4.42 \times 10^{-2}$	$2.08 \times 10^{-2}$
<b>median</b>	0.198	$6.08 \times 10^{-3}$	0.332	$4.42 \times 10^{-2}$	$1.14 \times 10^{-2}$
<b>standard deviation</b>	$4.31 \times 10^{-2}$	$1.11 \times 10^{-3}$	$5.21 \times 10^{-2}$	$3.66 \times 10^{-3}$	$2.86 \times 10^{-2}$
<b>minimum</b>	0.161	$5.14 \times 10^{-3}$	0.17	$3.87 \times 10^{-2}$	$5.81 \times 10^{-2}$
<b>maximum</b>	0.263	$7.12 \times 10^{-3}$	0.375	$5.40 \times 10^{-2}$	$9.87 \times 10^{-2}$

Table 6.3.5: Descriptive statistics of  $D$  by sample type.

and these were used to optimize thresholds.

### Samples Identified by Values of $D$

Sample Type	Thresholds		# of Samples Identified	
	Minimum	Maximum	Correctly	Incorrectly
HeNe	0.161	0.186	2	2
H	$5.14 \times 10^{-3}$	$5.15 \times 10^{-3}$	2	2
Hg	$0.214 \times 10^{-3}$	$0.375 \times 10^{-2}$	26	1
Lightbulb	$3.87 \times 10^{-2}$	$5.40 \times 10^{-2}$	28	0
Na	$5.81 \times 10^{-3}$	$1.66 \times 10^{-3}$	21	3
Totals			79	8
			90.8% correct	
			$p = 0.00017$ vs. $\mathcal{A}_{0.75}$	

Table 6.3.6: The  $p$ -value shows that sample identification with a strategy  $\mathcal{A}_{0.75}$ , that has an 75% probability of correctly identifying individual samples, would have less than a 0.017% chance of correctly identifying this many samples.

The second attempt at quantifying the trends in band gaps was the scalar  $G$ , which sorted the measurements at each position before looking for the jumps. The result identified 95.4% of the samples correctly.

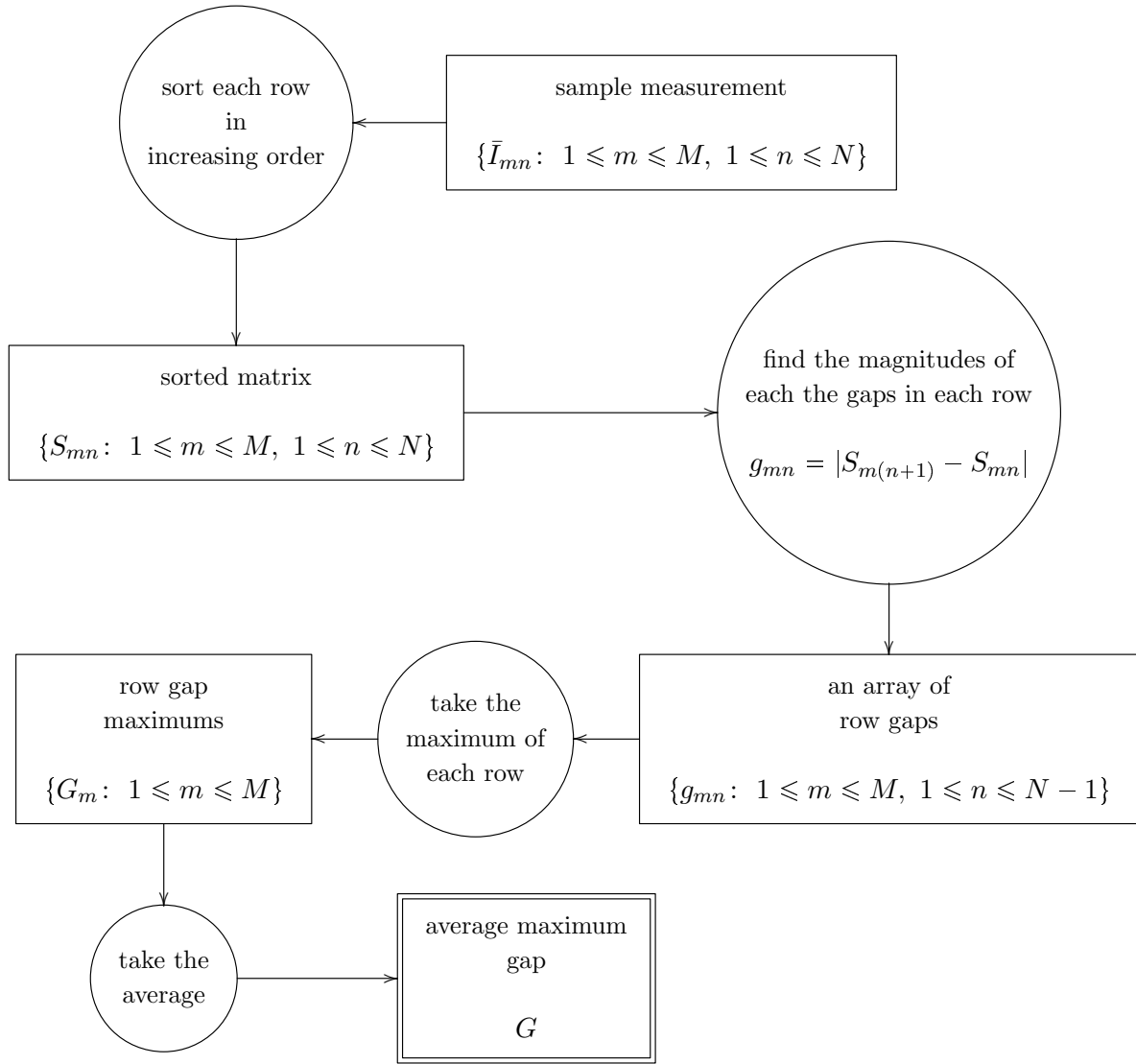


Fig. 6.3.7: Processing the scalar  $G$ , to quantify the trends in band gaps, initially sorted the intensities read at a given position. In this way it the presence of gaps in intensity readings from jumps in these readings occurring from one moment to the next. As with  $D$ , the effects of a background correction would have been nullified in the third step.

### $G$ by Sample Type (A.U.)

	HeNe	H	Hg	Lightbulb	Na
<b>mean</b>	0.131	$5.23 \times 10^{-4}$	$6.92 \times 10^{-2}$	$4.16 \times 10^{-3}$	$1.23 \times 10^{-3}$
<b>median</b>	0.118	$5.12 \times 10^{-4}$	$6.95 \times 10^{-2}$	$3.86 \times 10^{-3}$	$9.64 \times 10^{-4}$
<b>standard deviation</b>	0.124	$7.62 \times 10^{-5}$	$3.42 \times 10^{-2}$	$9.80 \times 10^{-4}$	$7.26 \times 10^{-4}$
<b>minimum</b>	$2.32 \times 10^{-2}$	$4.55 \times 10^{-4}$	$3.95 \times 10^{-3}$	$3.26 \times 10^{-3}$	$5.78 \times 10^{-4}$
<b>maximum</b>	0.263	$6.14 \times 10^{-4}$	0.125	$6.89 \times 10^{-3}$	$3.16 \times 10^{-3}$

Table 6.3.8: Descriptive statistics of  $G$  by sample type.

The specific thresholds used in the claim above were

### Samples Identified by Values of $G$

Sample Type	Thresholds		# of Samples Identified	
	Minimum	Maximum	Correctly	Incorrectly
HeNe	0.209	0.263	2	2
H	$4.55 \times 10^{-4}$	$6.14 \times 10^{-4}$	4	0
Hg	$8.53 \times 10^{-3}$	0.125	25	2
Lightbulb	$3.26 \times 10^{-3}$	$6.89 \times 10^{-3}$	28	0
Na	$5.78 \times 10^{-4}$	$3.17 \times 10^{-3}$	24	0
<b>Totals</b>			83	4
			95.4% correct	
			$p = 0.00208$ vs. $\mathcal{A}_{0.85}$	

Table 6.3.9: The  $p$ -value shows that sample identification with a strategy  $\mathcal{A}_{0.85}$ , that has an 85% probability of correctly identifying individual samples, would have less than a 0.21% chance of correctly identifying this many samples. The  $p$ -value of  $G$  vs.  $\mathcal{A}_{0.90}$  was 0.0566 which is just outside the significance of this level 0.05 test.

With so few mistakes in the identifications above, it would be easy to append conditional statements

to any of them in order to obtain 100% accuracy (because there were 204,800 data points per sample). But as stated at the outset, we're only looking for viable trends and don't want to overtrain on the data set.

## 7 Conclusions

---

The five main goals of this research have been to:

- i) Construct the static Fourier transform spectrometer, partially depicted in figure 1.0.2, from optical components and document the process step by step
- ii) Provide a complete overview of FT mathematics through measure theory and functional analysis, as is necessary to rigorously handle the spectroscopy performed with this device
- iii) Provide a complete map and analysis of the processing techniques used, from signal to spectra, in implementing the FT
- iv) Fourier transform interferograms measured with the spectrometer and analyze the results
- v) Investigate the potential for data-mining the new sets of data, quantify the results, and develop methods for assigning statistical significance to the results

Items ii) and iii) comprise their own sections in the main body above but we'll focus on the experimental results. The interferometer was successfully built eight times. Measurements were made with each build and cumulatively 87 interferograms were recorded from H, Hg, Na discharge lamps, a Sylvania lightbulb, and a HeNe laser. The Fourier transformed spectra are qualitatively distinct however two main issues inhibit this research from making statements on the quality of the static design.

- Collimated beams were produced from the non-coherent sources, but the quality of the collimation wasn't quantified and was most likely the greatest contributor to irregularities in the measured interferograms. Similarly the light sources had to be physically interchanged thus altering their beam path through the interferometer as well as the angle at which the interferogram is oriented on the detector.
- The primary concern with the construction, however, is that calibration with known spectra placed the FT spectrometer's resolution at an impractical  $3165\text{ cm}^{-1}$ : a factor of ten greater than is typically published (although these are mostly from Wollaston prism designs). Therefore the first steps in future FT work should be quantifying the resolution limits of this design, through calibration with known coherent sources, and expressing this in terms of the dimensions of the interferometer and optical components.

Moving on, the new time-resolved data output by the instrument showed many interesting trends in the behavior of interferograms. Three of these were quantified: time-variations, time discontinuities, and band-gaps in intensity. Each was shown capable of distinguishing sample types with over 90% accuracy. Band-gaps was the top performer and identified 95.4% of the samples correctly which, with the 87 samples measured, makes its performance significantly better ( $p = 0.00208$ ) than identifying the sources correctly with 85% probability. These results are particularly impressive as the measurements were made across 8 different interferometer builds and because of the optics issues mentioned above.

Additionally, the abundance of qualitative trends suggests that there is a lot of opportunity in data mining this new information. Going further with this requires targeting specific applications, and these can be selected for:

- Low risk to allow the mining of the new data to be eased into standard practice
- Field use to take advantage of the static interferometers inherent stability

The possibilities for data mining are also compounded by the engineering benefits of the instrument-low-cost, durability, and quick measurement time -which are ideal in most applications.

There's a question of whether the observed data trends can be attributed to sample types, the particular sources being used, or the interaction of these with the detector. However as these factors are always present and vary by application the point becomes moot. Indeed being able to recognize the specifics of the situation its in may be one of the instrument's greatest strengths.



## References

---

- [1] H. Aryamanya-Mugisha and R. R. Williams, “A Fourier Transform Diode Array Spectrometer for the UV, Visible, and Near-IR,” *Applied Spectroscopy*, vol. 39, no. 4, pp. 693–697, 1985.
- [2] M. Schardt, P. J. Murr, M. S. Rauscher, A. J. Tremmel, B. R. Wiesent, and A. W. Koch, “Static fourier transform infrared spectrometer,” *Opt. Express*, vol. 24, pp. 7767–7776, Apr 2016.
- [3] G. Boer, T. Scharf, and R. Dändliker, “Compact static fourier transform spectrometer with a large field of view based on liquid-crystal technology,” *Appl. Opt.*, vol. 41, pp. 1400–1407, Mar 2002.
- [4] A. Hegyi, “Birefringent static fourier-transform spectrometer for flow cytometry and imaging spectroscopy,” *Opt. Express*, vol. 25, pp. 17402–17410, Jul 2017.
- [5] M. Padgett and A. Harvey, “A static fourier-transform spectrometer based on wollaston prisms,” *Review of Scientific Instruments*, vol. 66, no. 4, pp. 2807–2811, 1995.
- [6] B. Patterson, M. Antoni, J. Courtial, A. Duncan, W. Sibbett, and M. Padgett, “An ultra-compact static fourier-transform spectrometer based on a single birefringent component,” *Optics Communications*, vol. 130, no. 1, pp. 1 – 6, 1996.
- [7] A. Lacan, F.-M. Bréon, A. Rosak, F. Brachet, L. Roucayrol, P. Etcheto, C. Casteras, and Y. Salaün, “A static fourier transform spectrometer for atmospheric sounding: concept and experimental implementation,” *Opt. Express*, vol. 18, pp. 8311–8331, Apr 2010.
- [8] G. Zhan, “Static Fourier-Transform Spectrometer with Spherical Reflectors,” *Applied optics*, vol. 41, no. 3, pp. 560–563, 2002.
- [9] J. Courtial, B. Patterson, B. Hirst, A. Harvey, A. Duncan, W. Sibbett, and M. Padgett, “Static fourier-transform ultraviolet spectrometer for gas detection,” *Applied optics*, vol. 36, pp. 2813–7, 06 1997.

- [10] A. A. Michelson and E. W. Morley, “On the Relative Motion of the Earth and the Luminiferous Ether,” *The American Journal of Science*, vol. 34, no. 203, pp. 333–345, 1887.
- [11] W. Rudin, *Real and Complex Analysis: 3rd Ed.* McGraw-Hill, 1986.
- [12] W. Rudin, *Analyse Fonctionnelle*. Ediscience, 1995.
- [13] D. Hearn, *Fourier Transform Interferometry*. MIT Lincoln Laboratory, 1999.
- [14] G. Chantry and J. Fleming, “Resolution Limits in Fourier Transform Spectrometry,” *Infrared Physics*, vol. 16, no. 6, pp. 655 – 660, 1976.
- [15] G. W. Ewing, *Analytical Instrumentation Handbook*. CRC Press, 1997.
- [16] J. R. Durig, *Analytical Applications of FT-IR to Molecular and Biological Systems: Proceedings of the NATO Advanced Study Institute Held at Florence, Italy, August 31 to September 12, 1979*, vol. 57. Springer Science and Business Media, 2012.
- [17] D. R. Lide, *CRC Handbook of Chemistry and Physics*. CRC press, 2009.